



OPEN ACCESS

EDITED BY

Sarah M. Hayes,
United States Geological Survey (USGS),
United States

REVIEWED BY

John Mavrogenes,
Australian National University, Australia
Leonid Danyushevsky,
University of Tasmania, Australia

*CORRESPONDENCE

Philip Rieger,
✉ phil.rieger.geo@gmail.com

SPECIALTY SECTION

This article was submitted to
Economic Geology,
a section of the journal
Frontiers in Earth Science

RECEIVED 09 March 2022

ACCEPTED 27 January 2023

PUBLISHED 27 February 2023

CITATION

Rieger P, Magnall JM, Gleeson SA and
Oelze M (2023), Pyrite chemistry records a
multistage ore forming system at the
Proterozoic George Fisher massive sulfide
Zn-Pb-Ag deposit, Mount Isa, Australia.
Front. Earth Sci. 11:892759.
doi: 10.3389/feart.2023.892759

COPYRIGHT

© 2023 Rieger, Magnall, Gleeson and
Oelze. This is an open-access article
distributed under the terms of the [Creative
Commons Attribution License \(CC BY\)](#).
The use, distribution or reproduction in
other forums is permitted, provided the
original author(s) and the copyright
owner(s) are credited and that the original
publication in this journal is cited, in
accordance with accepted academic
practice. No use, distribution or
reproduction is permitted which does not
comply with these terms.

Pyrite chemistry records a multistage ore forming system at the Proterozoic George Fisher massive sulfide Zn-Pb-Ag deposit, Mount Isa, Australia

Philip Rieger^{1,2*}, Joseph M. Magnall¹, Sarah A. Gleeson^{1,3} and
Marcus Oelze^{1,4}

¹GFZ German Research Centre for Geosciences, Potsdam, Germany, ²ICRAG SFI Research Centre in Applied Geosciences, University College Dublin, Dublin, Ireland, ³Institute of Geological Sciences, Freie Universität Berlin, Berlin, Germany, ⁴Federal Institute for Materials Research and Testing (BAM), Berlin, Germany

Trace element (TE) analysis of pyrite *via* LA-ICP-MS can be used to reconstruct the conditions of pyrite formation in complex mineral systems. The Carpentaria province in northern Australia is host to some of the world's highest value Zn-Pb (+Ag, Cu) deposits. The genesis of many of these deposits is controversial, with competing models of single- vs. multi-stage ore formation. In this study, LA-ICP-MS data of paragenetically constrained pyrite from the George Fisher Zn-Pb-Ag deposit has been analysed to investigate the chemistry of different stages of ore formation. Pyrite from correlative unmineralized host rocks has also been analysed to investigate evidence of distal hydrothermal anomalism. All LA-ICP-MS data have been statistically evaluated (principal component analysis) and interpreted together with whole rock litho-geochemical data of the same samples. Pre-ore diagenetic pyrite is compositionally similar to other Proterozoic diagenetic pyrite, with some evidence of minor hydrothermal anomalism that with further analysis could help define distal alteration. Pyrite from the different ore stages are compositionally distinct, consistent with a multi-stage system. Ore stage 1 pyrite exceeds background contents of Co, Cu, Zn, As, Ag, Sb, Tl, and Pb and has elevated Co/Ni ratios, whereas only Ni and Co are above background abundances in ore stage 2 and 3 pyrite, of which only ore stage 3 pyrite has high Co/Ni ratios. Ore stage 1 pyrite has a similar composition to hydrothermal pyrite in the undeformed northern Carpentaria CD-type deposits and was likely syn-diagenesis. Ore stage 2 was syn-deformation, and resulted in replacement and recrystallization of pre-existing pyrite, and the expulsion of incompatible TEs. Ore stage 3 formed *via* a later Cu-Zn-Pb mineralizing event that resulted in a new geochemically distinct generation of Co-rich pyrite. Overall, this study demonstrates the value of paragenetically-constrained pyrite TE data for refining genetic models in complex sediment hosted mineral systems.

KEYWORDS

CD-type massive sulfide deposit, pyrite chemistry, Proterozoic, LA-ICP MS, Mount Isa, Zn resources, mineral system, trace metals

1 Introduction

Pyrite is the most common sulfide mineral in the Earth's crust and can form in sedimentary, diagenetic, magmatic, metamorphic, and hydrothermal environments (ca. 0°C–700°C; e.g., Berner 1984; Craig and Vokes 1993). Pyrite chemistry provides an archive of isotopic and trace element (TE) information that can be used to reconstruct physicochemical conditions in these

diverse environments (e.g., Huerta-Diaz and Morse 1992; Fike et al., 2015; Keith et al., 2016). It is necessary to consider multiple different contributing factors when interpreting the TE composition of pyrite. For example, differing mechanisms of TE incorporation (e.g., substitution vs. mineral inclusion) have an intrinsic control on the composition of pyrite (Chouinard et al., 2005; Cook et al., 2009; Deditius et al., 2011). Similarly, element partitioning between different sulfide minerals in an equilibrium assemblage will also determine pyrite chemistry (Bethke and Barton, 1971; George et al., 2016; Grant et al., 2018). Pyrite chemistry may also be influenced by extrinsic factors that control fluid temperature and composition (e.g., Bajwah et al., 1987; Huston et al., 1995; Keith et al., 2016).

The early studies on pyrite chemistry relied on bulk methods to quantify TE composition (e.g., Huerta Diaz and Morse, 1992). In samples that are paragenetically complex, however, bulk methods will incorporate a mixture of pyrite generations with potentially different compositions. Over the last 20 years, technical advances in laser-ablation inductively coupled plasma mass spectrometry (LA-ICP-MS) now allow for the generation of large, high-resolution, TE pyrite chemistry datasets. For example, such datasets have been generated from sedimentary, diagenetic, and metamorphic pyrite (e.g., Large et al., 2014; Large et al., 2017; Ding et al., 2021) and from massive sulfide mineral deposits (e.g., Dehnavi et al., 2018; Gregory et al., 2019). Additionally, such high-resolution pyrite TE datasets can be used to reconstruct the spatial and temporal evolution of complex mineral systems (e.g., Maslennikov et al., 2009; Grant et al., 2018; del Real et al., 2020).

The majority of global Zn-Pb reserves are hosted by clastic-dominated-type (CD-type) Zn-Pb massive sulfide deposits. These deposits were historically referred to as sedimentary exhalative (SEDEX) deposits, however, as suggested by Leach et al., 2010, the CD-type terminology is favored as it does not have genetic connotations. The deposits are typically hosted in fine-grained pyritic rocks that can preserve a complicated sulfide paragenesis (Leach et al., 2005; Leach et al., 2010). Despite the potential utility of pyrite chemistry data, the number of high quality, paragenetically-constrained, CD-type pyrite chemistry datasets are limited (e.g., Gadd et al., 2016; Magnall et al., 2022).

Several of the world's highest value CD-type Zn-Pb deposits are located in the Carpentaria province in northern Australia (Figure 1; Leach et al., 2005; McGoldrick et al., 2010). In these deposits, pyrite occurs in pre-, syn-, and post-ore assemblages, and it has been used as a framework for paragenetic models. In the relatively undeformed CD-type deposits in the northern Carpentaria province, genetic models have described ore formation *via* exhalation of hydrothermal fluids during the deposition of the host rock (Mathias and Clark, 1975; Large et al., 1998) or epigenetic host rock replacement (Rye and Williams, 1981; Eldridge et al., 1993). Recent studies have shown that the Teena and neighbouring McArthur River (HYC) deposits formed during burial diagenesis (i.e., *via* syn-diagenetic replacement), based on petrographic, isotopic, mineralogical, geochemical, and structural data (e.g., Hayward et al., 2021; Magnall et al., 2021; Spinks et al., 2021). Importantly, in these two systems, ore stage pyrite is compositionally distinct from diagenetic pyrite, allowing for the development of TE vectors (Spinks et al., 2021; Magnall et al., 2022).

Tectonic overprinting has resulted in a more complicated sulfide paragenesis in CD-type deposits located in the southern Carpentaria province (e.g., Mount Isa, Hilton, and George Fisher deposits; Figure 1). At the Mount Isa deposit, the mineral system is

particularly complex and important to understand due to the formation of world class Zn-Pb- and Cu-ore bodies. As a result, debate has focused on whether the respective massive sulfide Zn-Pb and Cu(-Zn-Pb) ore bodies at the Mount Isa, Hilton, and George Fisher deposits formed during a single stage (e.g., McGoldrick and Keays, 1990; Perkins 1997; Cave et al., 2020a) or multiple stages (e.g., Heinrich et al., 1989; Valenta, 1994; Chapman 2004; Rieger et al., 2020a). Pyrite has formed throughout the paragenesis in these complex systems, although there is yet to be a detailed study that investigates pyrite TE chemistry. Indeed, recent petrographic, sulfur isotope, and whole rock litho-geochemical and mineralogical studies from the George Fisher deposit suggest that there are 3 generations of hydrothermal pyrite that are isotopically distinct, and that TE enrichment in un-mineralized rocks could be related to discrete pyrite alteration (Rieger et al., 2020b; Rieger et al., 2021). Since pyrite formed throughout the paragenesis in these complex systems, pyrite TE chemistry may lend important insight into the paragenetic history. Outstanding questions include whether pyrite preserves different TE chemistry between ore stages and whether there are similarities with the undeformed CD-type deposits of the northern Carpentaria province? To further investigate, we present paragenetically-constrained LA-ICP-MS TE data of pyrite from drill-core samples through the main ore bodies at the George Fisher deposit and from samples from a drill hole that intersected unmineralized, correlative host-rock lithologies (Urquhart Shale Formation).

2 Geological background

The Carpentaria province in northern Australia comprises sedimentary rocks that were deposited in two Paleo- to Mesoproterozoic intracontinental sedimentary basins (McArthur Basin and Mount Isa Inlier; Figure 1). These two sedimentary basins formed during the amalgamation of the Nuna (also known as Columbia) supercontinent (Betts et al., 2002; Betts et al., 2016; Giles et al., 2002). The regional stratigraphy is subdivided into three unconformity-bound depositional cycles, which developed in response to episodic rifting, sag phases, and basin inversions, and are further subdivided into twelve supersequences (Figure 1; Jackson et al., 2000; Southgate et al., 2013; Gibson et al., 2017). The major CD-type massive sulfide deposits (Figure 1A) are hosted within sedimentary rocks of the Gun, Loretta, River, and Doom supersequences, which belong to the Isa Superbasin (Figure 1; Southgate et al., 2000; Southgate et al., 2013). The onset of the Isan orogeny (ca. 1,600 Ma) led to basin closure and the rocks of the southern Mount Isa Inlier were deformed during multi-phase east-west and north-south deformation (Page and Bell, 1986; Connors and Page, 1995; Bell and Hickey, 1998).

The George Fisher (169 Mt at 9.0% Zn, 3.3% Pb, and 53 g/t Ag; Glencore, 2021), Hilton, and Mount Isa deposits are hosted by siltstones and mudstones of the Urquhart Shale Formation, which was deposited ca. $1,652 \pm 7$ Ma (Page and Sweet, 1998; Page et al., 2000) and is part of the Mount Isa Group (Figure 1D, Gun and Loretta supersequences; Southgate et al., 2000). The mudstones and siltstones are variably carbonaceous and pyritic but contain a high proportion of carbonate and feldspar (Neudert, 1983; Painter et al., 1999; Rieger et al., 2020b). It has been suggested that the Urquhart Shale Formation was deposited either in a carbonate slope (Neudert,

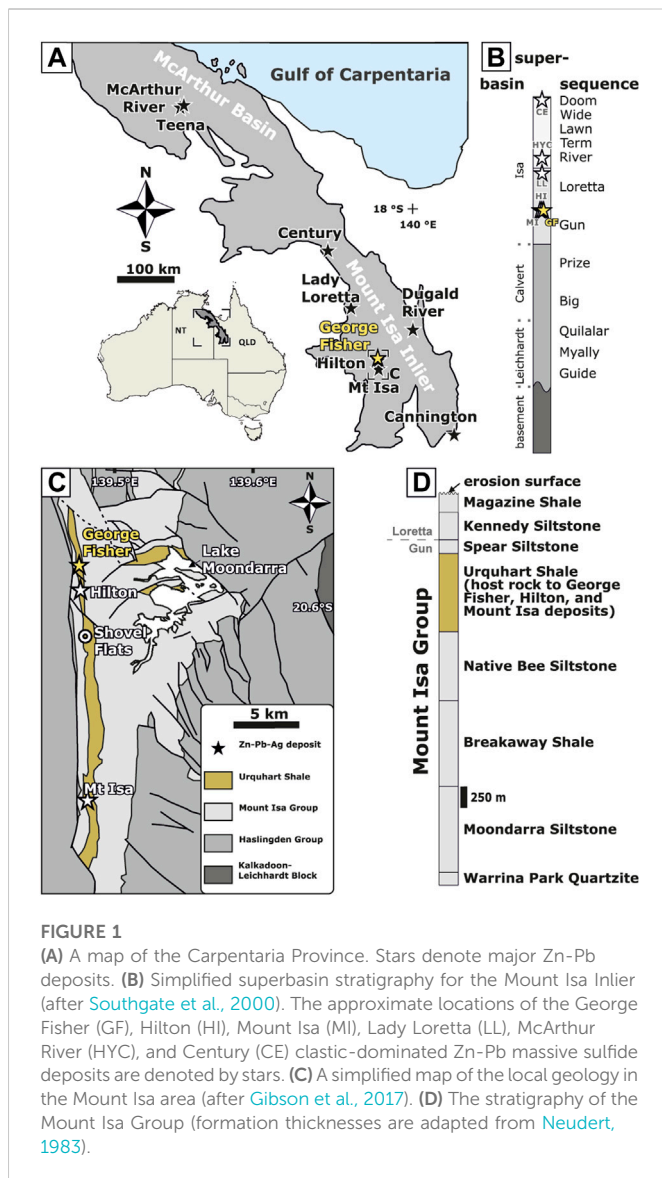


FIGURE 1

(A) A map of the Carpentaria Province. Stars denote major Zn-Pb deposits. (B) Simplified superbasin stratigraphy for the Mount Isa Inlier (after Southgate et al., 2000). The approximate locations of the George Fisher (GF), Hilton (HI), Mount Isa (MI), Lady Loretta (LL), McArthur River (HYC), and Century (CE) clastic-dominated Zn-Pb massive sulfide deposits are denoted by stars. (C) A simplified map of the local geology in the Mount Isa area (after Gibson et al., 2017). (D) The stratigraphy of the Mount Isa Group (formation thicknesses are adapted from Neudert, 1983).

1983; Painter, 2003) or a deeper-water slope (Domagala et al., 2000; Southgate et al., 2013) environment. Temperature constraints indicate that burial temperatures of the unmineralized Urquhart Shale distal to the Mount Isa and George Fisher deposits did not exceed 200°C–220°C (McClay, 1979; Chapman, 1999; Rieger et al., 2021).

The unmineralized Urquhart Shale Formation contains 2 types of pyrite; spheroidal to sub-spheroidal fine-grained (<10 μm) pyrite (Py-0) and coarser grained (up to several mm) euhedral pyrite (Py-euh) (Painter et al., 1999; Rieger et al., 2020a). The fine-grained pyrite is typically associated with carbonaceous laminations and preserves negative $\delta^{34}\text{S}$ values (Painter et al., 1999; Rieger et al., 2020a). The $\delta^{34}\text{S}$ values are similar to other analyses of pyrite from Proterozoic sedimentary basins (Lyons et al., 2014; Fike et al., 2015; Magnall et al., 2020) and consistent with pyrite formation *via* open system microbial sulfate reduction during early diagenesis (Rieger et al., 2020a). Moderate enrichment in total organic carbon (TOC <2 wt.%) and Mo (<30 ppm) is consistent with predominantly anoxic and ferruginous conditions during host rock deposition (Rieger et al., 2021; Rieger et al., 2022a). Coarser grained euhedral pyrite is

associated with carbonate veins and nodules that post-date the formation of fine-grained pyrite (Rieger et al., 2020a).

The main ore stage sulfide minerals in the George Fisher, Hilton, and Mount Isa massive sulfide deposits are pyrite, sphalerite, galena, chalcocopyrite, and pyrrhotite (e.g., Valenta, 1994; Chapman, 2004; Cave et al., 2020a; Cave et al., 2020b). At the George Fisher deposit it is generally accepted that sulfide mineralization formed epigenetically and during multiple stages (Chapman 1999; Murphy, 2004; Rieger et al., 2020a), although the volumetric importance of individual ore stages (syn-diagenetic vs. syn-deformation) and the relationship of Zn-Pb and Cu-Zn-Pb mineralization are not clear. There are no direct temperature constraints for the hydrothermal fluids at George Fisher (e.g., from fluid inclusions). Indirect temperature proxies (e.g., carbonate Eu/Eu* anomalies, chlorite thermometry, mineral twinning) indicate that hydrothermal mineralization occurred at temperatures of initially ca. 250°C–300°C, slightly lower than most temperature constraints for Mount Isa Cu mineralization (for more details on temperature constraints see Figure 3 in Rieger et al., 2021; Rieger et al., 2022a).

Whole-rock litho-geochemical data from George Fisher and unmineralized Urquhart Shale samples have been used to show how hydrothermal alteration and ore formation resulted in an enrichment of chalcophile elements (Ag, As, Cd, Co, Cu, Mo, Pb, Sb, Tl, Zn; Rieger et al., 2021). Some chalcophile elements (e.g., Tl and Ag) are enriched throughout all lithologies at George Fisher and co-vary with the pyrite abundance of the rock suggesting a correlation between TE enrichment and pyrite formation during hydrothermal fluid-rock interaction (Rieger et al., 2021). There is also evidence that ore stages may be associated with distinct TE compositions (e.g., Tl with ore stage 1; Rieger et al., 2021).

3 Methods

3.1 Sampling and petrography

A suite of representative samples were selected from 5 drill-cores, including 1 drill-core that intersected unmineralized Urquhart Shale (Shovel Flats drill-hole; $n = 91$) and 4 drill-cores that intersected the main ore bodies at the George Fisher deposit (drill hole 8C K751, $n = 61$; 10C K795, $n = 77$; 10C K798, $n = 57$; 12C I797, $n = 30$). The samples were selected from the main ore bodies, weakly mineralized sections, barren siltstones and mudstones, and, where possible, from hangingwall stratigraphy.

The samples were studied using a binocular microscope and 95 samples were chosen for polished thin section preparation. The thin sections were examined using transmitted- and reflected-light petrography and backscatter electron (BSE) imaging, see Rieger et al. (2020a) for details. Pyrite from a suite of representative samples was subsampled using a drill press and individual 2 mm pucks were mounted into 3 polished epoxy mounts, as described in Rieger et al. (2020a), which were also used for SIMS analysis.

3.2 Whole rock composition

The whole rock geochemical composition for samples used in this study was determined *via* ICP-MS, ICP-ES, X-ray fluorescence, and LECO analysis. The mineralogical composition was determined *via*

quantitative X-ray diffraction (XRD). For quality control and to determine pyrite abundances below detection limits of the XRD analysis, pyrite abundance was further also calculated from the molar concentrations of S, Pb, and Zn. For further details regarding the analytical methods see Rieger et al. (2020b); Rieger et al. (2021).

3.3 Electron probe micro-analyzer (EPMA)

Quantitative wavelength-dispersive spectrometry (WDS) of representative pyrite samples ($n = 22$) was carried out on a JEOL Superprobe JXA 8230 and a Hyperprobe JXA 8500F at the GFZ Helmholtz Centre Potsdam. Mounted samples and thin sections were carbon coated and 336 quantitative analyses of S, Fe, Co, Ni, Zn, As, and Pb were conducted at 15 keV, 20 nA, and a beam size of 1 μm . Counting times on the peaks were between 5 and 40 s. The instrument was calibrated on certified natural and artificial reference samples: pentlandite (Fe, Ni, S), sphalerite (Zn), galena (Pb), GaAs (As), and (Co, Ni)As₃ (Co) and ZAF-data correction was carried out. At these conditions, the detection limits were: 139 ppm for S; 149 ppm for Ni; 115 ppm for Co; 447 ppm for Zn; 132 ppm for As; and 499 ppm for Pb. Data were deemed acceptable at totals of 100 ± 3 wt.%.

3.4 Laser ablation inductively coupled plasma mass spectrometry (LA-ICP-MS)

In total, 1989 analyses were performed on pyrite from 28 samples contained within the 3 epoxy mounts and 16 additional polished thin sections. The LA-ICP-MS instrumentation comprised an Analyte Excite 193 nm ArF* excimer-based laser ablation (LA) system (Teledyne Photon Machines, Bozeman, MT, USA), coupled to a quadrupole-ICP-MS iCAP from Thermo Scientific. The LA-system is equipped with a HelEx II 2-volume ablation cell. Helium was used as a carrier gas for aerosol transport from the sample surface to the ICP and was mixed downstream with Ar as a make-up gas before entering the plasma. Operational parameters of the ICP-MS instrument and LA-unit were tuned for maximum sensitivity, low oxide formation based on the $^{232}\text{Th}^{16}\text{O}/^{232}\text{Th}$ ratio and low laser-induced elemental fractionation based on the $^{238}\text{U}/^{232}\text{Th}$ ratio using NIST SRM 610. Elements were calibrated using MASS1 as the certified reference material and ^{57}Fe as the internal standard. Samples were ablated for 30 s using a spot size between 20 and 30 μm , with a repetition rate of 10 Hz and an energy density of 2–3 J/cm². The data was reduced using the commercial software Iolite™ (Paton et al., 2011) and the data reduction scheme X_trace_elements_IS (Woodhead et al., 2007).

The fine grain size and complex paragenetic relationships of the sulfides meant a number of data processing procedures were necessary to ensure data quality. The time series for data integration (Figure 2) was carefully evaluated to ensure mixed ablations of pyrite and non-pyrite mineral phases were identified in the ablation profiles and rejected. Additionally, analyses with >5 wt.% Zn or Pb were rejected to reduce the influence of mixed analyses with sphalerite or galena. Data quality control resulted in the rejection of 338 and the retention of 1,651 pyrite analyses. The data quality was further confirmed following a comparison with electron probe micro-analysis (EPMA) data.

3.5 Statistical analysis

Statistical analysis of the TE dataset was carried out applying principal component analysis (PCA) using the software package ioGAS. Below limit of detection (LOD) values were imputed as 0.5*LOD of the respective analysis and the data ($n = 1,513$) were log transformed before applying a robust fast minimum covariance determination algorithm with an outlier cut-off of 0.975 and an alpha value of 0.75.

4 Results

4.1 Sulfide paragenesis

There are three types of sulfides at George Fisher: 1) pre-ore pyrite, 2) three stages of hydrothermal sulfides, and 3) pyrite that occurs in unmineralized rocks and likely formed post-ore. The relative timing of individual sulfides (paragenesis; Figure 3) has been described in detail by Chapman. (1999); Chapman. (2004) and Rieger et al. (2020a). The samples from Rieger et al. (2020a) are part of the sample set studied here and therefore, the same sulfide paragenesis was used in this study. In the following paragraphs, this paragenesis (Rieger et al., 2020a) is summarized with special emphasis placed on individual pyrite types and textures and, where possible, examples for paragenetic relationships of pyrite types within individual samples are shown.

Pre-ore pyrite (Py-0) occurs predominantly in laminated, carbonaceous siltstones of both background, unmineralized rocks (Py-0_{SF}; Figures 4A–D) and mineralized rocks at George Fisher (Py-0_{GF}; Figures 4E–L). Pyrite-0 occurs either as single grains or as grain aggregates (Figures 4G, K) and individual grains are generally very fine grained (<10 μm). This Py-0 typically consists of a (sub-) spheroidal core (Py-0a) and a subhedral to euhedral overgrowth (Py-0b; Figure 4H).

Ore stage 1 at George Fisher chiefly comprises sphalerite, pyrite (Py-1), and minor galena, which postdate and overgrow Py 0 (Figure 5). This ore stage is stratabound in laminated, carbonaceous siltstones and Py-1 is typically anhedral and occurs in 10 s–100 s μm sized nodules and nodular beds (Figure 5).

Ore stage 2 occurs as breccias and veins, in which the matrix mostly consists of galena, sphalerite, pyrrhotite and pyrite. The pyrite (Py-2) is euhedral and 50–500 μm in size (Figure 6). In ore stage 2 samples the host rock and previous sulfides are typically replaced (Figure 6D), deformed (Figures 6A–C), and crosscut (Figures 6E–G).

Ore stage 3 formed either stratabound massive sulfide units or veins and breccias that crosscut all previous lithologies and sulfides. The main sulfide minerals are pyrrhotite and pyrite (Py-3), but galena, sphalerite, and chalcocopyrite are also present in the veins and breccias (Figure 7). This ore stage is volumetrically minor and spatially restricted to the western part of the deposit. It is also the only sulfide assemblage that contains chalcocopyrite and it is often associated with buff cream-coloured phyllosilicate alteration of the host rock that is distinct from other alteration assemblages at George Fisher (Figure 7E). Pyrite (Py-3) is typically coarse grained (>100 μm) and euhedral to subhedral (Figures 7C, G). During this ore stage previous sulfides were typically replaced or deformed (e.g., Py-1; Figure 7D).

The timing of large (100 s μm) euhedral pyrite (Py-euh) and of hangingwall pyrite (Py-HW) relative to the ore stage sulfides is not well constrained as they only occur in unmineralized rocks. These two generations of pyrite typically occur in late carbonate veins and nodules that postdate Py-0 and are likely post-ore.

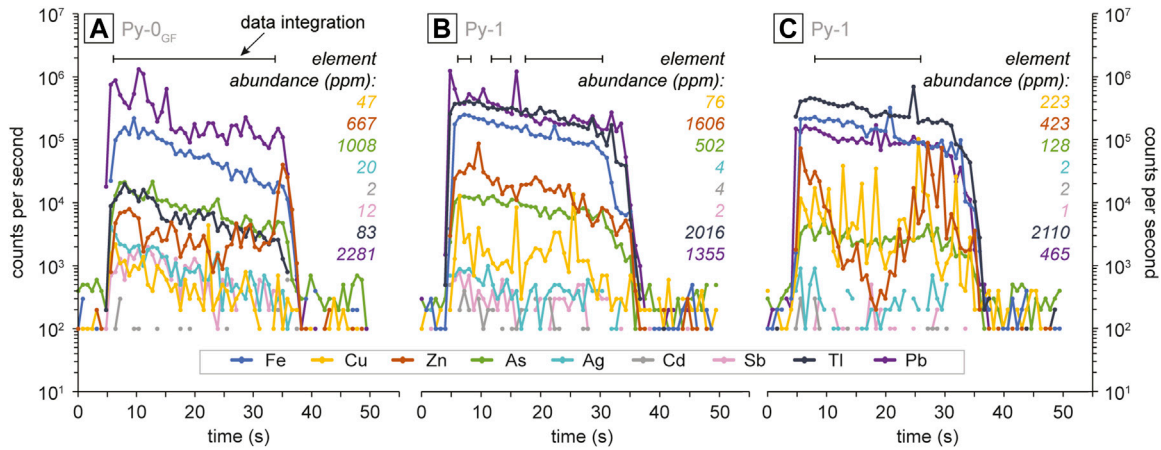


FIGURE 2 Time-resolved LA-ICP-MS profiles of representative analyses of (A) Py-0 from George Fisher (Py-0_{Gf}) and of Py 1 (B,C). The colours represent individual elements, the areas selected for data integration are denoted by black bars above the ablation profiles, and element abundances for the individual analyses are reported in the respective colours.

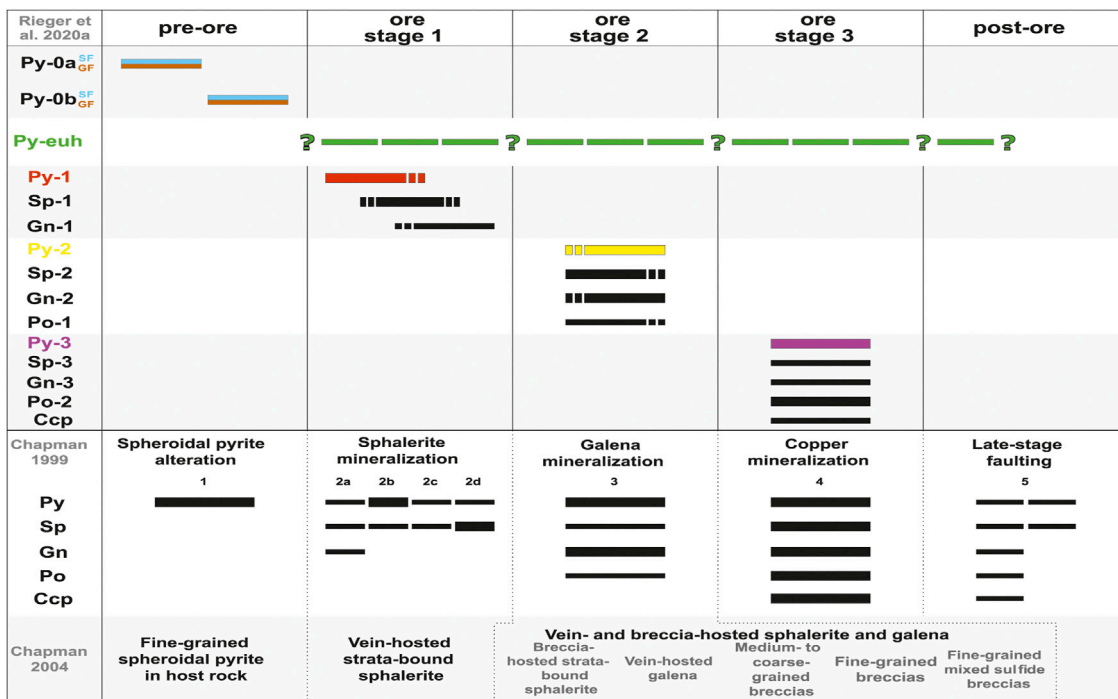


FIGURE 3 The paragenetic sequence of sulfide minerals at the George Fisher deposit as determined by Chapman (1999, 2004) and Rieger et al. (2020a); modified after Rieger et al., 2020a). The individual bars show the relative timing of sulfides and bar thickness denotes the abundance within respective sulfide stages. Mineral abbreviations are: chalcocopyrite (Ccp), galena (Gn), pyrrhotite (Po), pyrite (Py), and sphalerite (Sp).

Paragenetically constrained sulfur isotope data indicate that 1) Py-0 formed from reduced sulfur produced *via* open system microbial sulfate reduction, 2) reduced sulfur for Py-1, Py-3, and Py-euh was derived *via* thermochemical sulfate reduction, whereas 3) Py-2 formed *via* the replacement, recycling, and recrystallization of pre-existing Py-0 and Py-1 (Rieger et al., 2020a).

4.2 Pyrite trace element chemistry

There is a general overlap between EPMA and LA-ICP-MS data for analyses that are above the EPMA detection limits (Figures 8A–C). Within individual pyrite types the variability of some LA-ICP-MS element abundances is higher than the variability of EPMA data (Figure 8; e.g., Zn, As, Pb in Py-2 and Py3). These wider LA-ICP-

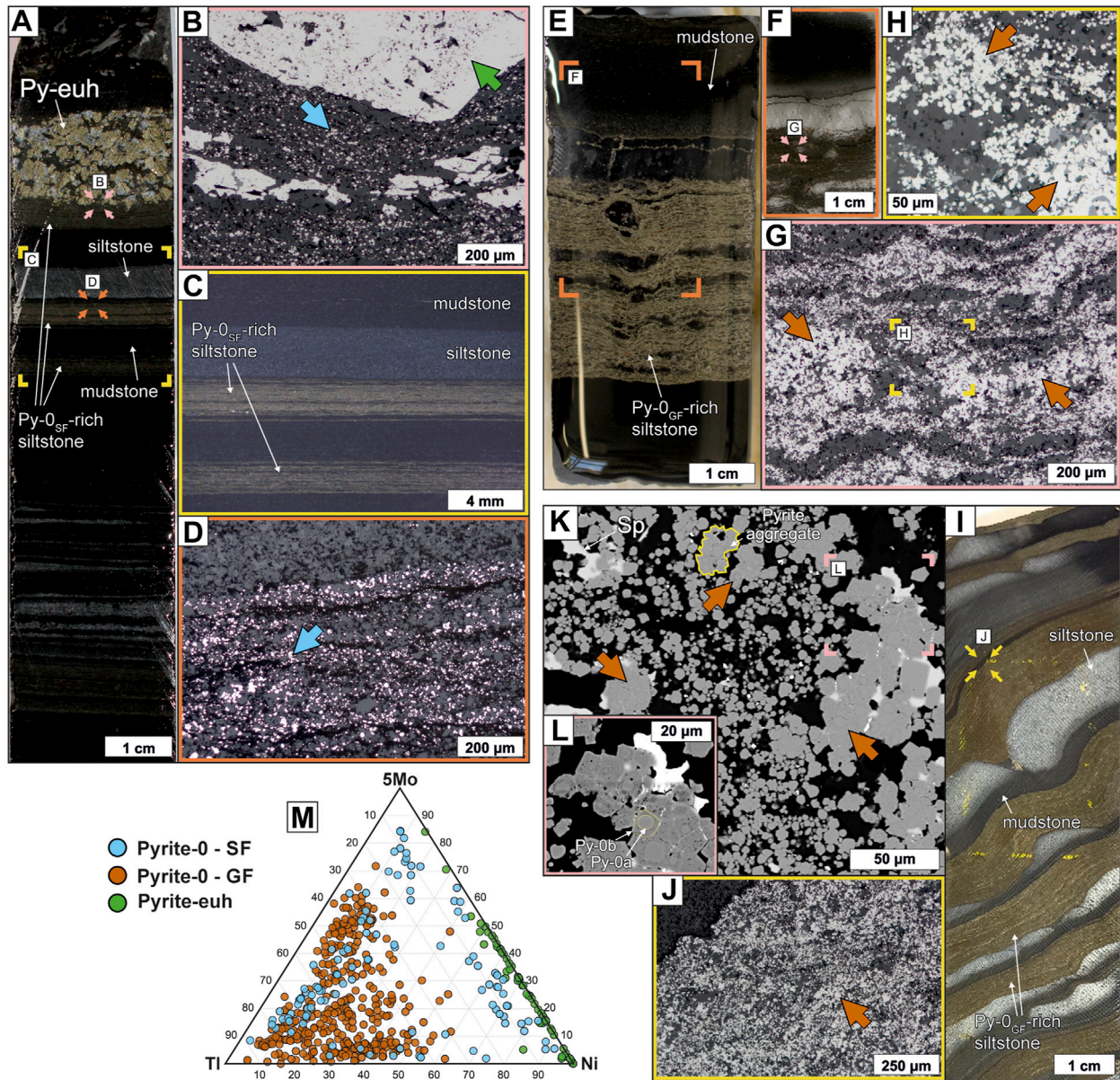
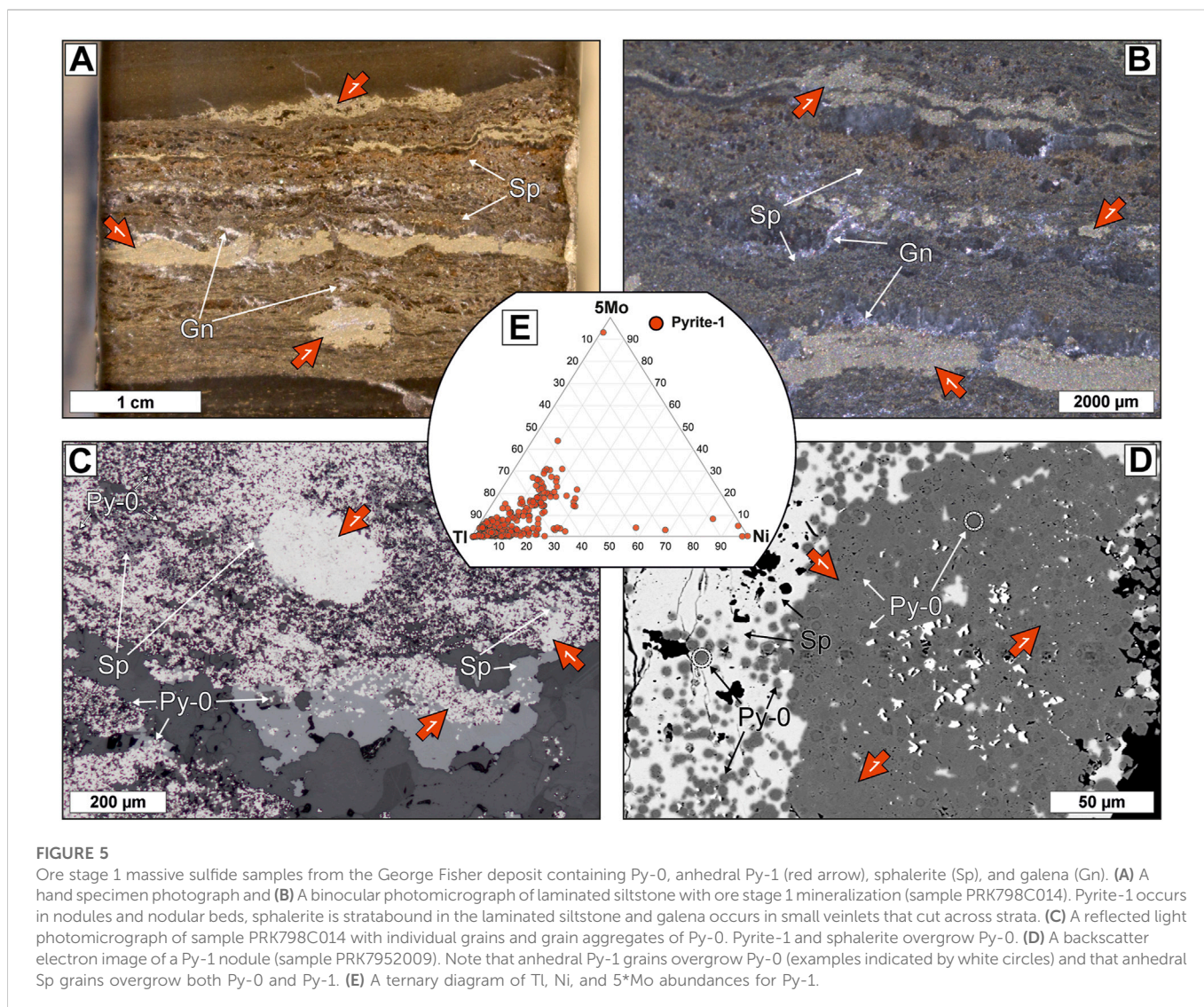


FIGURE 4

Urquhart Shale samples containing abundant fine-grained Py-0 [Shovel Flats drill-core: (A–D), George Fisher deposit: (E–L)]. (A) A hand specimen photograph of sample PR832SF040 containing Py-0_{SF}-rich (Py-0 from the Shovel Flats drill hole) laminae and Py-euh. The coloured rectangles and arrows denote the location of (B–D). (B) A reflected light photomicrograph of Py-0_{SF} (blue arrow) and Py-euh (green arrow). (C) A binocular photomicrograph of laminated siltstone with abundant Py-0_{SF}. (D) A reflected light photomicrograph of Py-0_{SF} (blue arrow). (E) A hand specimen photograph of sample PRK7952023 containing Py-0_{GF}. The orange rectangle denotes the location of (F). (F) A photograph of a thin section of sample PRK7952023 containing Py-0_{GF} (dark brown laminae). The pink arrows denote the location of (G). (G) A reflected light photomicrograph of Py-0_{GF} (brown arrows), which is present in individual grains and grain aggregates. The yellow rectangle denotes the location of (H). (H) A reflected light photomicrograph of Py-0_{GF} (brown arrows). (I) A hand specimen photograph of sample PRK751003 containing laminated, carbonaceous Py-0_{GF}-rich siltstone (brown with yellow striations), calcite- and dolomite-cemented siltstone (light grey to white), and carbonaceous mudstone (dark grey to black). The yellow arrows denote the location of (J). (J) A reflected light photomicrograph of abundant Py-0_{GF} (Py-0 at George Fisher) in laminated siltstone. (K) A backscatter electron photomicrograph of Py-0_{GF} (brown arrows) and minor sphalerite (Sp). Pyrite-0_{GF} is either present in individual grains or grain aggregates. The pink rectangle denotes the location of (L). (L) A backscatter electron photomicrograph of a Py-0_{GF} aggregate. Note the zonation of individual grains with spheroidal to sub-spheroidal cores (Py-0a) and euhedral to subhedral overgrowths (Py-0b). (M) A ternary diagram of Tl, Ni, and 5*Mo abundances for Py-0_{SF}, Py-0_{GF}, and Py-euh.

MS data distributions are likely due to: 1) the higher numbers of samples and analyses compared to EPMA; and 2) the lower detection limit for LA-ICP-MS. The LA-ICP-MS data are therefore considered more representative of the individual pyrite types than the EPMA data. The abundances of individual TEs vary across orders of magnitude

(10 ppm–5 wt.%) and TE abundances of individual pyrite types can vary significantly (see median and median absolute deviation in Table 1). The most abundant TEs are Zn, As, and Pb, which are most enriched in Py-1, have intermediate abundances in Py-0, and are generally depleted in Py-2, Py-3, Py-euh, and hanging wall pyrite



(Table 1; Figures 8A–C). The remaining TEs (Mn, Co, Ni, Cu, Mo, Ag, Sb, and Tl) account for less than half of the total TE budget, but there is major variability in the relative proportions of these elements among the different generations of pyrite (Table 1; Figure 9). Contents of Mn and Sb are highest in Py-0 from the Shovel Flats drill hole (Py-0_{SF}; Figure 9B). Manganese is also high in Py-0 at George Fisher (Py-0_{GF}; Figure 9C) and Mn contents of Py-1 are low (Figure 9D). Molybdenum is highest in Py-0_{SF} and Py-0_{GF} (Figures 9B, C) and intermediate in Py-1 (Figure 9D). Contents of Sb are highest in Py-0_{SF}, high in Py-1, and intermediate in Py-0_{GF} (Figures 9C–E). Abundances of Mn, Mo, and Sb are lowest in Py-2 and Py-3 (Figures 9E, F). Thallium is most abundant in Py-1 (Figure 9D), intermediate in Py-0_{SF} and Py-0_{GF} (Figures 9B, C), and lowest in Py-2 and Py-3 (Figures 9E, F). The abundances of Ag are highest in Py-0_{GF} and Py-1 (Figures 9C, D) and low in Py-0_{SF}, Py-2, and Py-3 (Figures 9B–F). Abundances of Cu and Co are highest in Py-1 (Figure 9D), although relative to the other TEs the proportions of Cu and Co are highest in Py-0_{SF} (Figure 9B) and Py-3 respectively (Figure 9F). The abundance of Ni is constant throughout all generations of pyrite (median = 33–88 ppm; median_{all-data} = 58 ppm; MAD_{all-data} = 38 ppm), but its relative proportion to the other TEs is much higher in Py-2

(Figure 9E). The full LA-ICP-MS pyrite dataset is available in a datafile (Rieger et al., 2022b) and a summary of the data is shown in Table 1.

The abundances of most TEs (Mn, Co, Cu, As, Mo, Ag, and Sb) in Py-0_{SF} and Py-0_{GF} are similar to median values for sedimentary and diagenetic pyrite from the Proterozoic ($0.25 < \text{Py-0}/\text{Py}_{\text{Proterozoic}} < 4$; Figure 10A; Large et al., 2014). Significant TE enrichment ($\text{Py-0}/\text{Py}_{\text{Proterozoic}} > 4$) and depletion ($\text{Py-0}/\text{Py}_{\text{Proterozoic}} < 0.25$) in Py-0_{SF} and Py-0_{GF} is only indicated for Zn and Tl, and Ni, respectively (Figure 10A). Pyrite-0_{GF} is also enriched in Pb and depleted in Cu (Figure 10A). Relative to literature values for SEDEX pyrite (Gregory et al., 2019), ore stage 1 pyrite (Py-1) has anomalous Tl and Pb enrichment ($\text{Py-1}/\text{Py}_{\text{SEDEX}} > 4$) similar to hydrothermal pyrite from the Teena deposit (McArthur basin, northern Carpentaria province; Magnall et al., 2022). Hydrothermal Py-1 is also significantly enriched in Zn and Co and has similar TE abundances to SEDEX pyrite in Cu, As, Ag, and Sb. Whereas Py-2 and Py-3 are depleted in all TE except for Co and are therefore distinct from SEDEX or Teena pyrite (Figure 10B).

A principal component analysis shows that 66.7% variance of the dataset can be described by the first 2 principal components (PC1 and

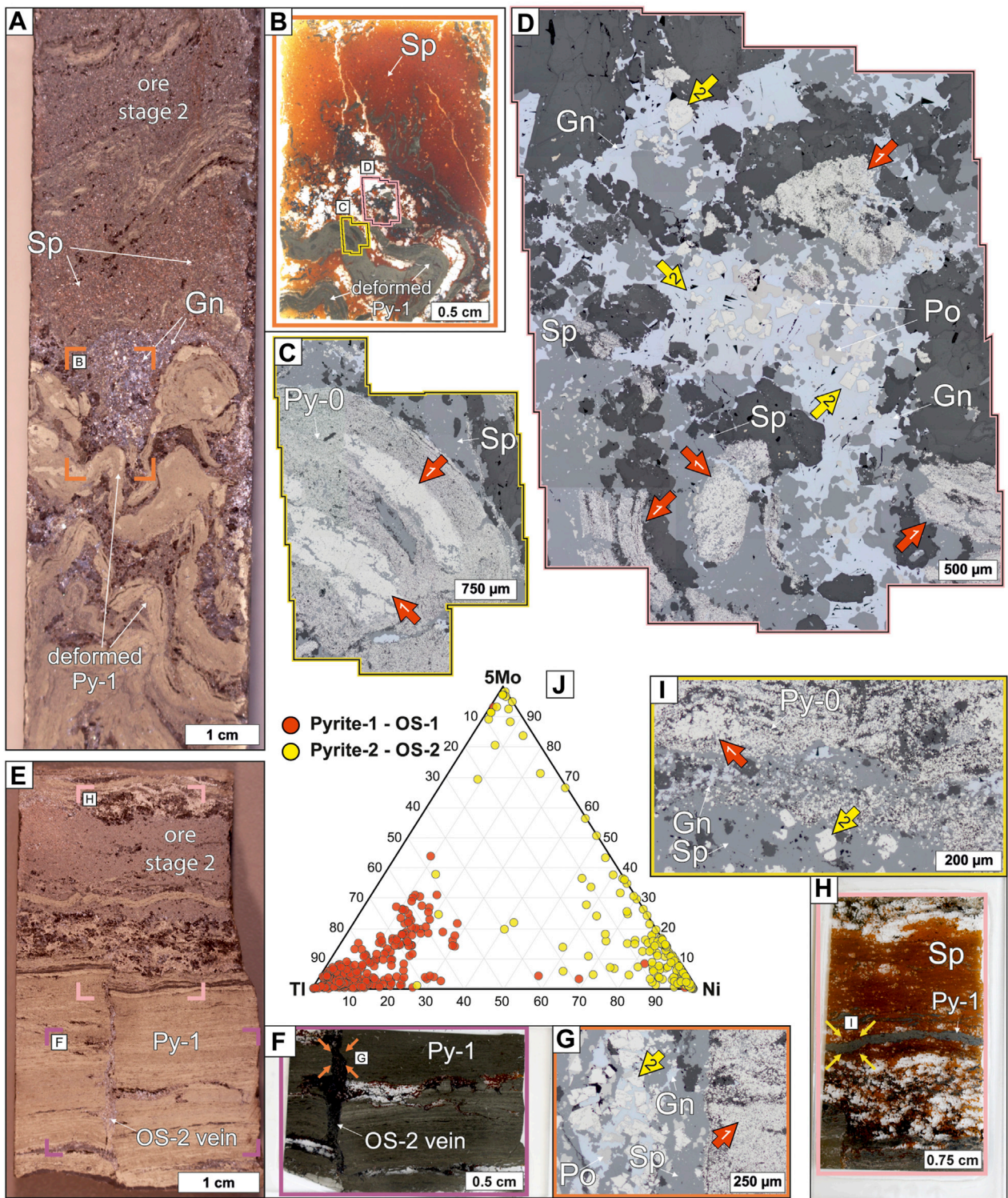


FIGURE 6
 Ore stage 1 and 2 massive sulfide samples from the George Fisher deposit containing anhedral Py-1, euhedral Py-2, sphalerite (Sp), galena (Gn), and pyrrhotite (Po). **(A)** A hand specimen photograph of sample PRK798C013. The orange rectangle denotes the location of **(B)**. **(B)** A photograph of a thin section of deformed Py-1 in a massive sphalerite (Sp) breccia. The yellow and pink polygons denote the location of **(C,D)**, respectively. **(C)** A reflected light photomicrograph of deformed Py-1 (red arrows). **(D)** A reflected light photomicrograph of deformed, Py-1 (red arrows), which is cross-cut and replaced by ore stage 2 sphalerite (Sp), galena (Gn), and pyrrhotite (Po), and euhedral Py-2 (yellow arrows). **(E)** A hand specimen photograph of sample PRK798C011. The purple and pink rectangles denote the location of **(F,H)**, respectively. **(F)** A photograph of a thin section of an ore stage (OS) 2 vein that cross-cut Py-1. The orange arrows denote the location of **(G)**. **(G)** A reflected light photomicrograph of Py-1 (red arrow) cross-cut by an ore stage (OS) 2 vein containing euhedral Py-2, sphalerite (Sp), galena (Gn), and pyrrhotite (Po). **(H)** A photograph of a thin section of an ore stage 2 breccia containing euhedral Py-2, sphalerite (Sp), galena (Gn, not labelled), and pyrrhotite (Po, not labelled). The yellow arrows denote the location of **(I)**. **(I)** A reflected light photomicrograph of ore stage 2 sphalerite (Sp), galena (Gn), and euhedral Py-2 (yellow arrow) that have replaced and infilled after anhedral Py-1 (red arrow). **(J)** A ternary diagram of Ti, Ni, and 5*Mo abundances for Py-1 and Py-2.

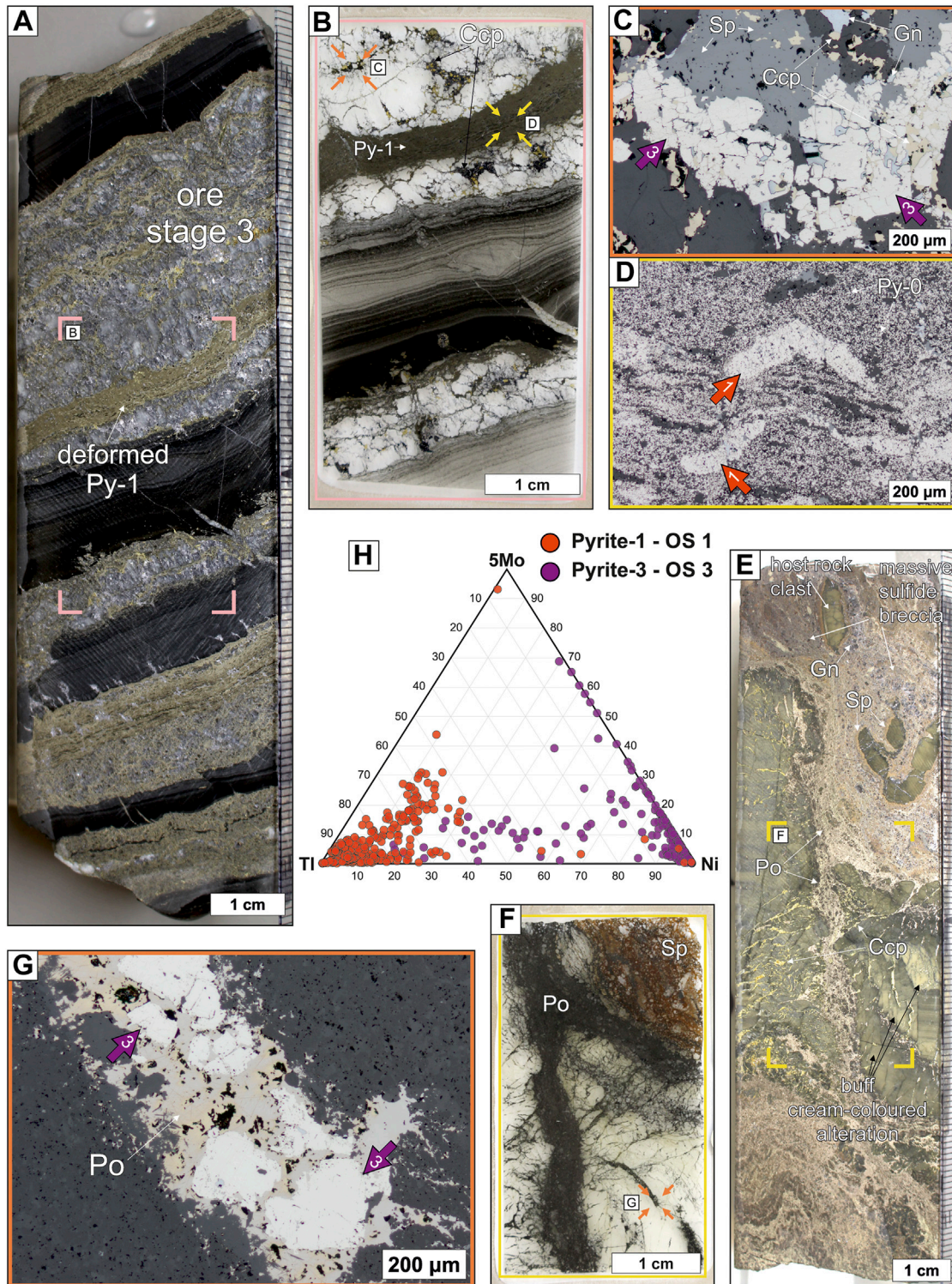


FIGURE 7

Ore stage 1 and 3 sulfide samples from the George Fisher deposit containing euhedral to subhedral Py-3, sphalerite (Sp), galena (Gn), pyrrhotite (Po), and chalcopyrite (Ccp). (A) A hand specimen photograph of sample PRK751041 with deformed anhedra Py-1 and with an ore stage 3 vein. The pink rectangle denotes the location of (B). (B) A photograph of a thin section of an ore stage 3 vein with deformed Py-1. The orange and yellow arrows denote the locations of (C,D), respectively. (C) A reflected light photomicrograph of ore stage 3 coarse grained euhedral to subhedral Py-3 (purple arrows), sphalerite (Sp), galena (Gn), and chalcopyrite (Ccp). (D) A reflected light photomicrograph of deformed Py-1 (red arrows). (E) A hand specimen photograph of sample PRK751049 with an ore stage 3 breccia with pyrrhotite (Po), chalcopyrite (Ccp), galena (Gn), and sphalerite (Sp). Note the buff cream-coloured host rock alteration which is typical for, and restricted to, ore stage 3 at George Fisher. The yellow rectangle denotes the location of (F). (F) A photograph of a thin section of an ore stage 3 breccia and veins. The orange arrows denote the location of (G). (G) A reflected light photomicrograph of an ore stage 3 vein with pyrrhotite (Po) and coarse grained euhedral to subhedral Py-3 (purple arrows). (H) A ternary diagram of TI, Ni, and 5*Mo abundances for Py-1 and Py-3.

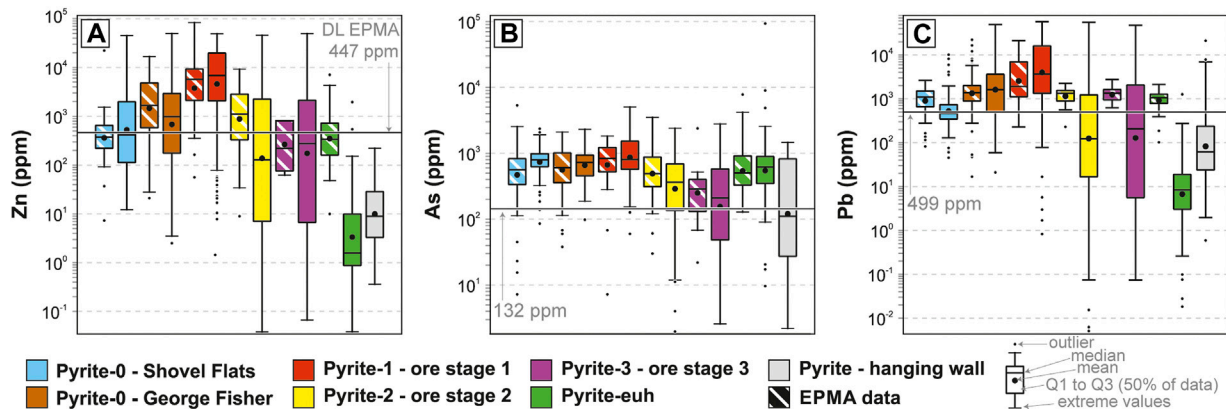


FIGURE 8

The abundance of Zn (A), As (B), and Pb (C) for individual pyrite sub-groups determined via LA-ICP-MS and EPMA. The black lines in (A–C) denote respective EPMA detection limits (DL). The total number of samples and analyses of LA-ICP-MS (28 samples, 1,651 analyses) exceeds that of EPMA (22 samples, 336 analyses). Note that EPMA results for below detection limit values are reported here but have large uncertainties. Shown are also statistical details for box and whisker plots used in this study.

PC2; Figures 11A–C). The group of minor TEs (Mn, Co, Ni, Cu, Mo, Ag, Sb, and Tl) are separated into three sub-groups in PC1–PC2 space. The major TEs (Zn, As, and Pb) cluster with Ag, Cu, Sb, and Tl, but with lower scaled coordinates for PC1. Principal component 2 is best described by the variance of the elements Mn and Mo (scaled coordinates ca. 0.7) and Ni and Co (scaled coordinates ca. –0.6 and –0.8; Figure 11A). With respect to the individual pyrite generations, PC1 values are high for Py-1 (median = 1.5), intermediate for Py 0 (median ca. 0.4) and low for all other pyrite generations (median < –2.5; Py-2, Py-3, Py-euh, and hangingwall pyrite (Py-HW); Figure 11B). The values for PC2 are high (median ≥ 1) for Py-0 and low for all other pyrite generations (median < 0; Py 1, Py-2, Py-3, Py-euh, and Py-HW; Figure 11C).

Using three of the elements (Tl, Mo, and Ni) from the different subgroups in PC1–PC2 provides a tool to visualize differences in TE composition among paragenetic stages of pyrite (Figure 11D). Py-0 data are intermediate between the endmembers, whereas Py-1 data are concentrated at the Tl endmember, and Py-2 and Py-3 data are located at the Ni endmember (Figure 11D). Pyrite-euh and Py-HW data are distributed between the Mo and Ni endmembers and overlap only with Py-2 and Py-3, but not with Py-0 and Py-1 (Figure 11D).

4.3 Degree of trace metal pyritization (DTMP)

In this study, the DTMP is calculated using the median abundance of TE in pyrite (TE_{pyrite}) as determined by LA-ICP-MS, the whole rock TE abundance (TE_{wr}), and the whole rock pyrite abundance ($pyrite_{wr}$; Rieger et al., 2021).

$$DTMP = \left(TE_{pyrite} * pyrite_{wr} \right) / TE_{wr}$$

The DTMP in samples containing only Py-0 from George Fisher and the Shovel Flats drill hole are reasonably comparable, whereas DTMP values in samples containing different proportions of ore stage pyrite are much more variable (Figure 12). In most samples (except for

those containing Py-euh and Py-HW), the DTMP for Mn and Zn is generally low (<10%) and high for Co, Ni, and As (>45%). In samples that mostly contain Py-0, the DTMP is high for Cu (>25%), Mo (>25%), Ag (>50%), Sb (ca. 100%), Tl (>50%), and Pb (>25%). Pyrite contains a large proportion of the whole rock budget of Cu (>25%) and Tl (>50%) for samples with dominantly Py-1 and an intermediate proportion for Py-1+Py-2-dominant samples (Cu = 20%; Tl = 40%), whereas those elements are mainly hosted by other phases in Py-3-, Py-euh-, and Py-HW-dominant samples (<10%). The DTMP of Mo, Ag, Sb, and Pb is generally low or intermediate (0%–25%) for Py-1-, Py-2-, Py-euh-, and Py-HW-dominant samples, whereas in Py-3-dominant samples pyrite contains an intermediate to high proportion of the Mo-, Ag-, Sb-, and Pb-budget (20%–140%). Significant outliers occur for Co contents in Py-3 samples and for Ag in Py-0 samples.

5 Discussion

The George Fisher deposit formed from multiple episodes of hydrothermal activity, which has resulted in a complex sulfide paragenesis (e.g., Figures 3, 5–7; Chapman, 2004; Murphy, 2004; Rieger et al., 2020b). It has already been established from bulk rock analyses that pyrite is one of the main host phases for some TEs (e.g., Tl; Rieger et al., 2021), and the generation of *in situ* LA-ICP-MS data provides more precise constraints on the composition of different generations of pyrite. A number of factors may have contributed to the TE chemistry of different stages of pyrite formation. These factors may have operated on the small scale (<μm–cm), i.e., substitution and inclusion mechanisms of individual TEs and their fractionation between co-precipitating sulfides. Additionally, TE geochemistry may have also been influenced by larger scale factors such as fluid temperature and fluid/metal source(s). To investigate this further, the following discussion will evaluate the TE mass balance by comparing the data generated *in situ* (LA-ICP-MS) with existing whole rock compositional data; this is then followed by a discussion of the individual factors controlling pyrite geochemistry at different paragenetic stages and the implications for ore genesis at the George Fisher deposit.

TABLE 1 Summary of LA-ICP-MS results.

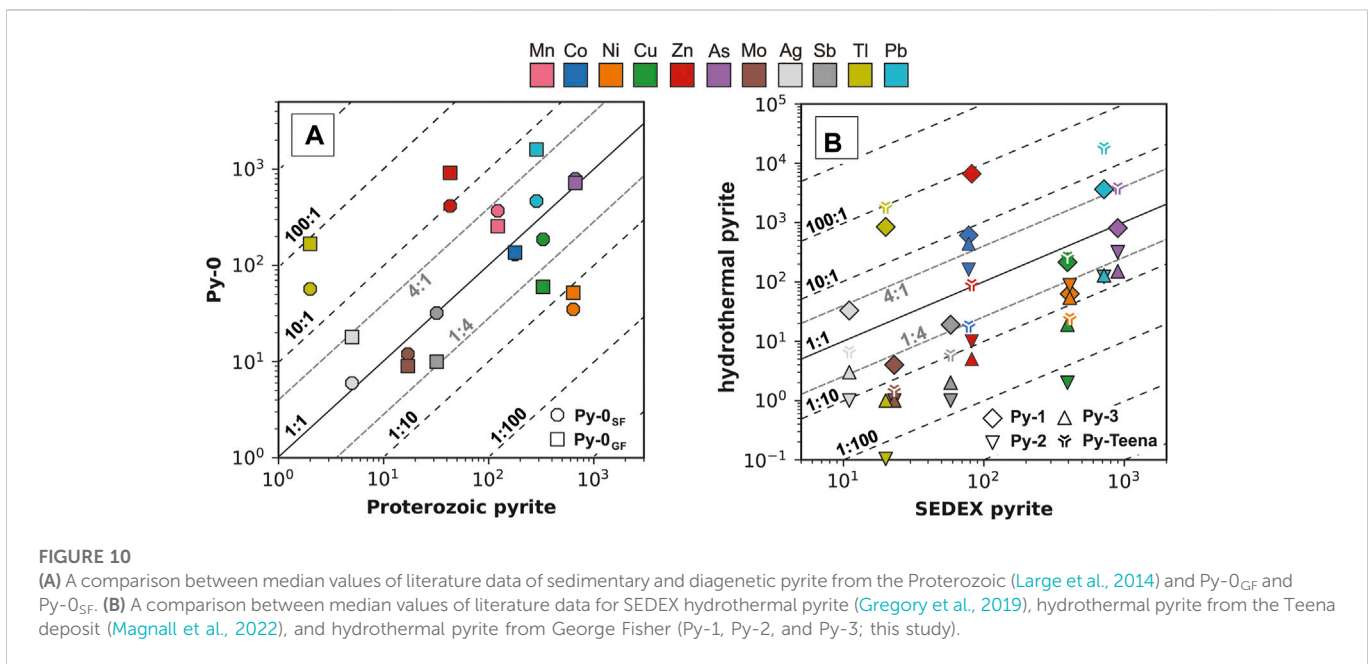
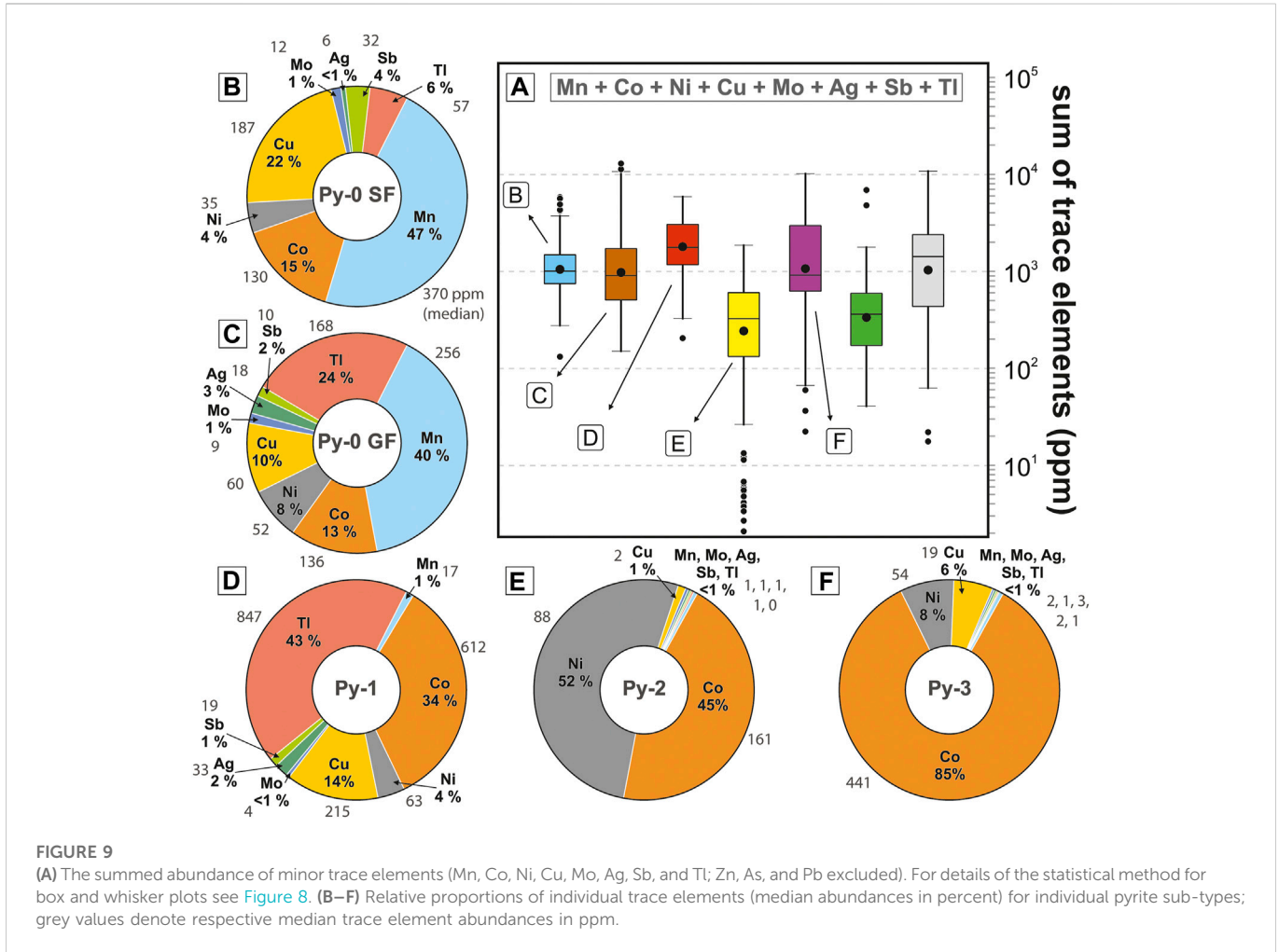
Pyrite (n)	Mn	Co	Ni	Cu	Zn	As	Mo	Ag	Sb	Tl	Pb	Sum	sum _{major}	sum _{minor}	Co/Ni	Main TE characteristics
Py-0 _{SF} (112)	370	130	35	187	415	795	12	6	32	57	467	3,284	2,022	1,010	2.4	Zn and Tl > Proterozoic ¹ ; Ni < Proterozoic ¹
MAD	149	62	19	67	367	178	5	3	12	46	156					
Py-0 _{GF} (387)	256	136	52	60	917	721	9	18	10	168	1,605	5,866	4,075	911	1.9	Zn Tl, and Pb > Proterozoic ¹ ; Ni and Cu < Proterozoic ¹
MAD	139	115	35	37	883	244	3	8	5	120	1,164					
Py-1 (392)	17	612	63	215	6,653	808	4	33	19	847	3,652	19,743	17,362	1,763	10.1	Co, Cu, Zn, As, Ag, Sb, Tl, Pb, and sum > Py-0; high Co/Ni; Co, Zn, Tl, and Pb > SEDEX ² ; Ni and Mo < SEDEX ²
MAD	7	413	31	159	6,148	347	2	11	8	422	2,895					
Py-2 (335)	1	161	88	2	10	317	1	1	1	0	122	1,844	1,334	337	1.3	Co and Ni > Py-0; low Co/Ni; All TE except Co < SEDEX ²
MAD	0	154	62	1	10	247	0	1	1	0	119					
Py-3 (213)	2	441	54	19	5	151	1	3	2	1	129	3,365	718	891	7.4	Co and Ni > Py-0; high Co/Ni; All TE except Co < SEDEX ²
MAD	2	385	36	18	5	147	0	3	2	1	129					
Py-euh (82)	0	157	33	1	1	617	1	0	0	0	8	1,088	643	314	7.6	Co > Py-0; high Co/Ni
MAD	0	150	19	1	1	272	1	0	0	0	7					
Py-HW (130)	1	134	952	9	3	37	1	1	8	0	62	1,766	320	1,441	0.3	Ni > Py-0; low Co/Ni
MAD	1	94	696	7	2	34	1	1	5	0	54					
LOD	2	1	1	3	3	6	0.1	0.1	0.2	0.02	0.2					
Proterozoic ^a	122	178	638	329	43	668	17	5	32	2	285					
SEDEX ^b		78	409	394	82	899	23	11	58	20	717					
Py-Teena ^c	95	18.1	24.3	263	90	3,840	1.49	6.7	5.9	1,830	18,300					

Median abundance and MAD (median absolute deviation) per pyrite type (in ppm); median limits of detection (LOD) per element (in ppm); median total sum, sum of major TE (Zn+As+Pb), sum of minor TE (Mn+Co+Ni+Cu+Mo+Ag+Sb+Tl) per pyrite type (in ppm); Co/Ni ratios and main TE characteristics per pyrite type. Literature data:

^aLarge et al. (2014)

^bGregory et al. (2019)

^cMagnall et al. (2022).



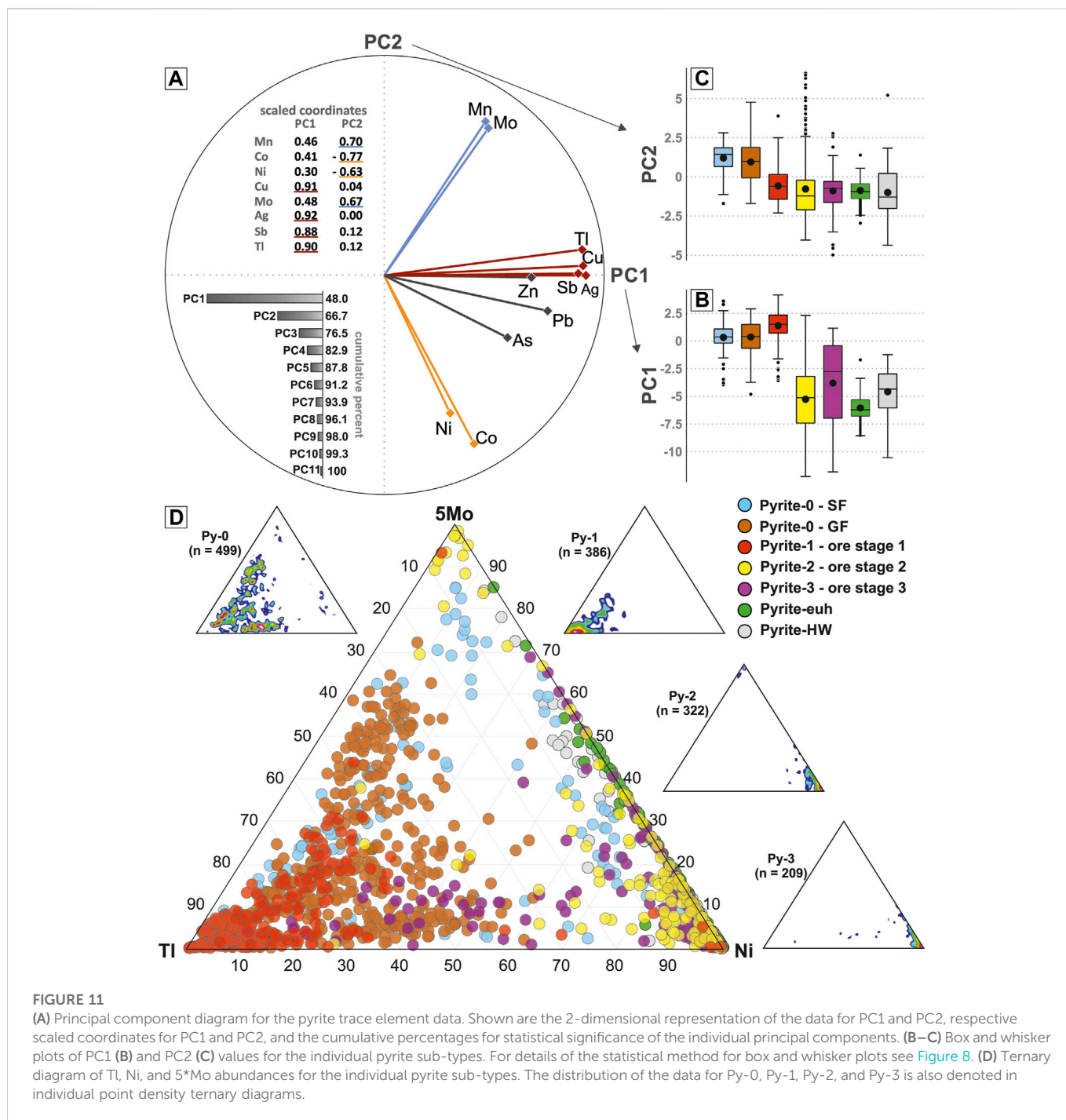


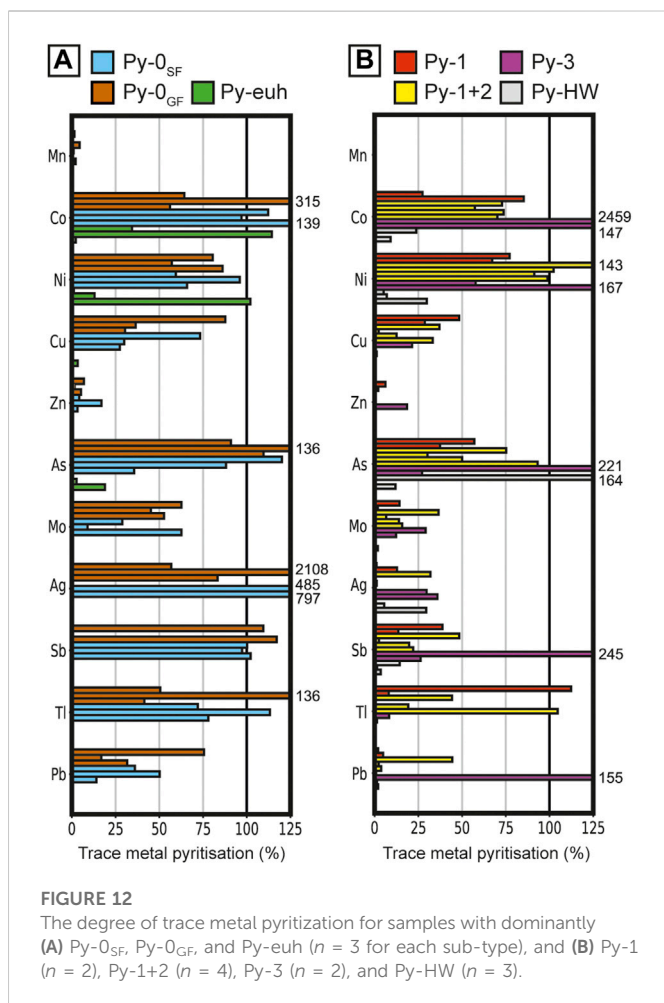
FIGURE 11

(A) Principal component diagram for the pyrite trace element data. Shown are the 2-dimensional representation of the data for PC1 and PC2, respective scaled coordinates for PC1 and PC2, and the cumulative percentages for statistical significance of the individual principal components. (B–C) Box and whisker plots of PC1 (B) and PC2 (C) values for the individual pyrite sub-types. For details of the statistical method for box and whisker plots see Figure 8. (D) Ternary diagram of Tl, Ni, and 5*Mo abundances for the individual pyrite sub-types. The distribution of the data for Py-0, Py-1, Py-2, and Py-3 is also denoted in individual point density ternary diagrams.

5.1 Whole rock vs. LA-ICP-MS pyrite chemistry

The degree of trace metal pyritization (DTMP) represents the proportion of TEs in the whole rock that are present in pyrite. Previous studies have focused on organic rich sediments and calculated the DTMP following the analysis of TEs in the whole rock and a separate chemical extraction of pyrite (Huerta-Diaz and Morse, 1990; Huerta-Diaz and Morse, 1992). The samples from George Fisher have a more complicated paragenesis and the

whole rock and LA-ICP-MS data have been generated on different scales. Specifically, the LA-ICP-MS data were generated at the thin section scale, whereas whole rock data was produced from 15 to 20 cm drill core intervals (Rieger et al., 2021). This may help to explain some of the variability in the DTMP values, although there are still some useful general observations to make. For example, the DTMP values that strongly exceed 100% likely represent compositional values for pyrite that are not representative of the whole rock pyrite composition. This could be attributed to a) mixed ablations comprising pyrite and minor TE rich sulfide



inclusions or b) the presence of a second, TE poor, but volumetrically abundant, type of pyrite in a sample (e.g., Py-0 vs. Py-euh). The low DTMP values then highlight the TEs that are hosted by other mineral phases (e.g., Zn in sphalerite; Mn in carbonate).

Given these uncertainties, samples from Shovel Flats and George Fisher that only contain Py-0 have DTMP values for most TEs that are reasonably comparable (i.e., consistently low, e.g., Mn = 0–4%; consistently intermediate, e.g., Pb = 14–76%; consistently high, e.g., Sb = 97–117%) in (Figure 12A), which confirms pyrite chemistry is relatively homogenous between these samples. The low DTMP_{Mn} values indicate that pyrite was only a minor sink for Mn, which is likely to be primarily incorporated into carbonate (Rieger et al., 2021). Intermediate to high DTMP_{Mo} values (averages: Shovel Flats = 33%; George Fisher = 53%; Figures 12A, B) indicate that a large fraction of Mo is incorporated into pyrite, although a significant proportion may also be associated with organic matter in the host rock (e.g., Chappaz et al., 2014). Interpreting DTMP values in ore stage samples is more complicated, due to multiple generations of pyrite and other TE rich sulfide phases (e.g., sphalerite, galena, chalcocopyrite). The outlier DTMP values that exceed 100% (e.g., Co, Ag, Sb; Figures 12A, B) indicate the ablation of pyrite that is not representative of the whole rock composition. They could also be generated by the ablation of mineral inclusions of other sulfide

phases that could incorporate those elements (e.g., galena, chalcocopyrite, sphalerite, sulfosalts) or by the presence of low volume TE rich pyrite overgrowths (e.g., Li et al., 2022; Magnall et al., 2022). Conversely, the low DTMP of Zn, Pb, and Cu, indicates that the whole rock budget of these metals is associated primarily with sphalerite, galena and chalcocopyrite respectively. Despite variability among individual ore stages, high DTMP for Co, Ni, As, and Tl (Figure 12) do indicate that these elements are dominantly hosted by pyrite.

5.2 Mechanisms of trace element incorporation into pyrite

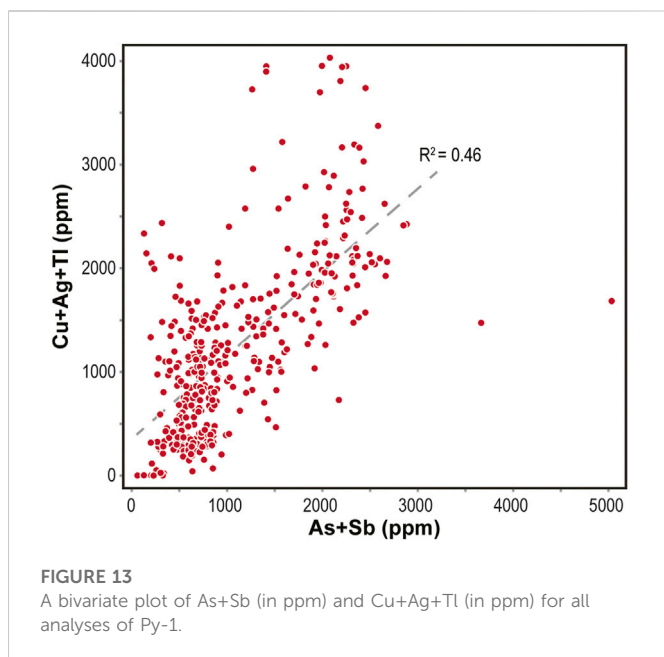
Trace element incorporation into pyrite is complex and may be controlled by several factors, including: isovalent or heterovalent substitution into the crystal lattice (e.g., Chouinard et al., 2005), nano to microscopic mineral inclusions (e.g., Deditius et al., 2011), or as a combination of both (e.g., Cook et al., 2009). These different mechanisms of TE incorporation are likely reflected by the three element groupings in the PCA (Figure 11A): 1) Mn and Mo, 2) Cu, Zn, As, Ag, Sb, Tl, and Pb, and 3) Co and Ni.

5.2.1 Mn & Mo

In low temperature, diagenetic environments, pyrite is the long-term sink for a suite of TEs (e.g., Co, Ni, Cu, As, Mo, Sb, Tl; Raiswell and Plant, 1980; Huerta-Diaz and Morse, 1992; Morse and Luther, 1999). The correlation between Mn and Mo is likely attributable to authigenic processes. The main flux of reactive Mn in marine sediments is associated with Mn⁴⁺ oxide phases that form complexes with a suite of TEs (e.g., Mo) in seawater (e.g., Nameroff et al., 2002; Dellwig et al., 2010; Scholz, 2018). The reduction of Mn⁴⁺ in anoxic sediments occurs before sulfate reduction and the build-up of reduced sulfur in pore fluids. As a result, carbonate is the main sink for Mn²⁺ in reducing sediments, consistent with the low DTMP values in the samples from George Fisher and the Shovel Flats drill hole. However, when there is a high amount of sulfide in pore fluids Mn²⁺ is preferentially incorporated into pyrite (Morse and Luther, 1999). The release of Mo during the reduction of Mn⁴⁺-oxides also results in the scavenging of Mo by Fe sulfides and organic matter (Huerta Diaz and Morse, 1992; Helz et al., 1996; Vorlicek et al., 2004). Locally, higher DTMP_{Mo}, and slightly higher DTMP_{Mn}, of Py-0_{GF} relative to Py-0_{SF} may indicate that the availability of reduced sulfur was higher at George Fisher (e.g., Vorlicek et al., 2018), which is consistent with slightly more restricted conditions with respect to reduced sulfur indicated by sulfur isotope values of Py-0_{SF} (Rieger et al., 2020a).

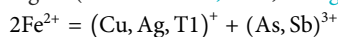
5.2.2 Cu, Zn, As, Ag, Sb, Tl, & Pb

The abundances of these metals in the pyrite may be due to a combination of nano-inclusions (Pb, Ag, Zn) and coupled heterovalent lattice substitution (Tl, As, Cu, Sb). The different ionic radii of Fe²⁺ (0.61 Å) and Pb²⁺ (1.19 Å) mean that isovalent substitution is unlikely (D'Orazio et al., 2017) and therefore, the Pb could be present as homogeneously distributed nanoparticle inclusions (e.g., Deditius et al., 2011), which is consistent with relatively smooth ablation profiles for Pb in Py-1 (Figures 2B, C). However, the spatial resolution of LA-ICP-MS analyses (>10 μm) means it is difficult to



separate homogeneously distributed nano-inclusions from lattice substitution (Reich et al., 2016) and we cannot resolve this issue.

In contrast, heterovalent substitution involving As^- and As^{3+} for S^{2-} and Fe^{2+} can have an important control on TE incorporation into pyrite (e.g., Deditius et al., 2008; Deditius and Reich, 2016; Kusebauch et al., 2019). Heterovalent substitution results in unbalanced charge and distortions in the crystal lattice of pyrite, which allow for the effective incorporation of other monovalent or trivalent TEs (e.g., Tl^+ , Cu^+ , Ag^+ , Sb^{3+} ; e.g., Reich et al., 2005; Deditius et al., 2008; Qian et al., 2013). The covariation of Cu, Ag, and Tl vs. As and Sb in Py-1 (Figure 13) may indicate a coupled substitution of these elements for Fe^{2+} during pyrite formation in ore stage 1 (D’Orazio et al., 2017; George et al., 2018):



A combined and homogeneous substitution is consistent with relatively smooth ablation profiles for As and Tl (Figures 2B, C). The uneven ablation profiles of Cu, Ag, and Sb could indicate that these elements are either heterogeneously distributed in the crystal lattice or that they occur in micro-inclusions. To further refine element deportment future studies should apply $< \mu\text{m}$ -scale analytical techniques (e.g., synchrotron analysis).

5.2.3 Co & Ni

Cobalt is typically positively correlated with Ni in sedimentary pyrite (Gregory et al., 2016). In diagenetic environments, both metals are directly incorporated into Fe monosulfides (e.g., Scholz and Neumann, 2007) and will also substitute directly for Fe^{2+} into the crystal structure of pyrite (Maslennikov et al., 2009). As Co and Ni tend to be incorporated equally, the Co/Ni ratio of pyrite has been used to classify the origin and source of fluids associated with pyrite formation (Bajwah et al., 1987). Diagenetic pyrite typically preserves Co/Ni ratios less than 1, whereas higher Co is associated with magmatic and/or hydrothermal systems related to mafic sources (e.g., Bajwah et al., 1987). The overall high Co/Ni ratios (≥ 1) of diagenetic and hydrothermal pyrite from George Fisher and Shovel Flats may mean that they may have a common hydrothermal affinity, whereas low Co/Ni ratios may indicate a non-hydrothermal affinity (e.g., Py-HW;

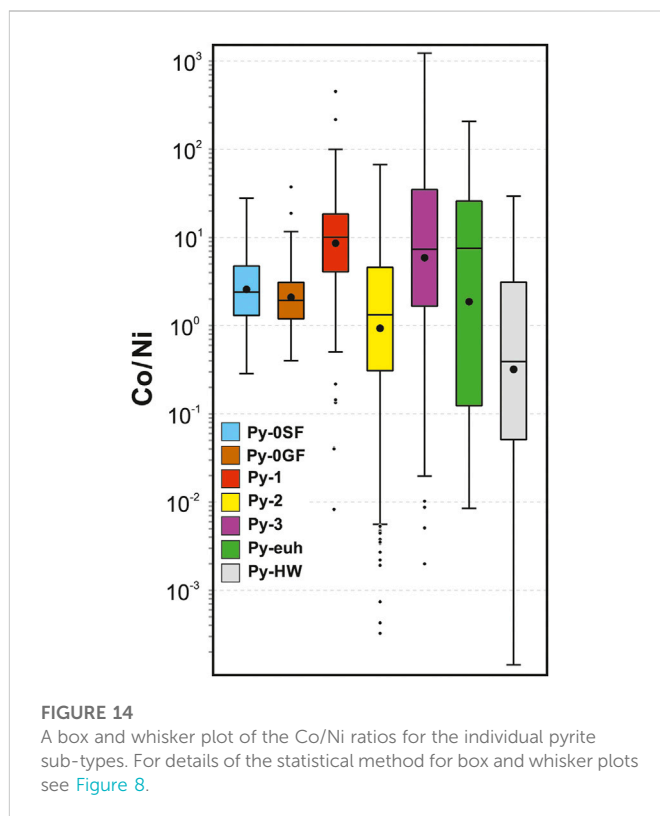


Figure 14). For diagenetic Py-0 this hydrothermal Co/Ni signature could result from low-volume hydrothermal overgrowths on pyrite (e.g., Li et al., 2022; Magnall et al., 2022). Alternatively, high Co/Ni ratios may have also resulted from Ni-depleted conditions during early diagenesis and Py-0 formation, which is consistent with Ni depletion relative to literature data for Proterozoic sedimentary and diagenetic pyrite (Figure 10A). High Co/Ni ratios in Py-1, Py-3, and Py-euh (Figure 14) are most indicative of hydrothermal Co-enrichment (Bajwah et al., 1987) and also consistent with Co-enrichment relative to literature data for hydrothermal SEDEX pyrite (Figure 10B). In contrast, low Co/Ni ratios in Py-2 and Py-HW (Figure 14) likely are the result of another process. Most TEs (As, Sb, Tl, Pb, Zn, Ag) are effectively removed during recrystallisation of pyrite, however, Co and Ni are most compatible and may remain in the pyrite lattice (George et al., 2018).

5.3 Paragenetic evolution of ore stage pyrite chemistry

The distinctive composition of pyrite in each of the ore stages records useful information about the genesis of the George Fisher deposit. Pyrite-1 has high Co/Ni ratios and above background concentrations ($> \text{Py-0}$) of Co, Cu, Zn, As, Ag, Sb, Tl, Pb, and TE totals (Figures 8–10, 14; Table 1). Pyrite-2 and Py-3 have above background concentrations of Co and Ni, and Py-2 has low Co/Ni ratios, whereas Co/Ni ratios of Py-3 are high (Figures 8–10, 14; Table 1). Pyrite-1 is similar or enriched relative to hydrothermal pyrite from the northern Carpentaria province, except for Ni and Mo, whereas Py-2 and Py-3 are depleted in all TE except for Co (cf., Gregory et al., 2019; Magnall et al., 2022).

5.3.1 Ore stage 1

Ore stage 1 at George Fisher formed *via* syn-diagenetic replacement (Chapman, 2004; Murphy, 2004; Rieger et al., 2020b) and the mineralization is texturally and compositionally similar to the ore stage mineralization in the undeformed CD-type deposits in the McArthur Basin (e.g., Eldridge et al., 1993; Spinks et al., 2021; Magnall et al., 2022). In these undeformed deposits, hydrothermal pyrite formed spheroidal or anhedral crystals, as well as overgrowths on diagenetic pyrite (Eldridge et al., 1993; Spinks et al., 2021; Magnall et al., 2022). These pyrites are often zoned and exhibit enrichments in a number of TEs (e.g., Tl, As, and Pb; Magnall et al., 2020; Spinks et al., 2021), which likely occurred due to heterovalent substitution of those elements in the crystal structure of hydrothermal pyrite (Magnall et al., 2022).

Nucleation of hydrothermal pyrite on pre-existing diagenetic pyrite is a common feature of sub-seafloor replacement (e.g., Piercey, 2015; Nozaki et al., 2021). The interaction of hot hydrothermal fluids with the cooler host rocks (temperature difference ca. 50°C–100°C; Rieger et al., 2021; Rieger et al., 2022a) may have resulted in growth rates that exceeded the rate of equilibration and removal of TEs. This may have allowed for the effective incorporation of TEs (inclusions and substitutions) and is consistent with high TE abundances (Figures 8, 9) and coupled heterovalent substitution of As+Sb and Tl+Cu+Ag (Figure 13). Furthermore, it is also consistent with the porous and anhedral textures of Py-1 (Figures 5–7; for more details on pyrite morphology see also Rieger et al., 2020b), and with high sulfate consumption/supply rates during thermochemical sulfate reduction as indicated by highly variable sulfur isotope values (Rieger et al., 2020a).

5.3.2 Ore stage 2

During deformation, ore stage 2 sulfides formed *via* the replacement and recycling of pre-existing pyrite, which is evidenced by replacement textures and intermediate sulfur isotope values relative to pre-existing pyrite generations (Py-0 and Py-1; Rieger et al., 2020a). Both Py-0 and Py-1 have much higher TE abundances and a more diverse TE composition than Py-2 (Figures 4–6, 8, 9; Table 1). This may mean that less compatible TEs were effectively removed during replacement and recrystallization of pre-existing pyrite, which resulted in TE-poor and relatively Ni-Co-dominated Py-2 (Figures 6, 9). Cobalt and Ni are commonly retained during recrystallization, whereas other TEs are removed from pyrite and either precipitated as sulfosalts or removed and transported within the fluids (D'Orazio et al., 2017; George et al., 2018). Such sulfosalts have so far not been described at George Fisher, but they would likely be volumetrically minor (<0.1 mol of As+Tl+Sb per kg recrystallized Py-1) and may be extremely challenging to detect in most systems (George et al., 2018).

5.3.3 Ore stage 3

Ore stage 3 pyrite (Py-3) is associated with the Cu mineralization at George Fisher (Figure 7; Rieger et al., 2020b) and the TE composition of Py-3 is clearly different to Py-0 and Py-1, and slightly more similar to Py-2 (Figures 8–11; Table 1). The high Co/Ni ratios together with the absence of most other TEs in Py-3 suggests that it formed from a separate hydrothermal event, which is consistent with the distinctly different sulfur isotope values compared to ore stage 1 and 2 (Rieger et al., 2020a). High Co/Ni ratios in pyrite may also indicate that the metals were derived from a mafic source rock (Bajwah et al., 1987). Indeed, it has been suggested that Mount Isa Cu was

sourced from mafic volcanic rocks in the sequences below the deposits (Eastern Creek Volcanics; e.g., Heinrich et al., 1989; Hannan et al., 1993). Sphalerite and chalcopyrite associated with Cu-mineralization at Mount Isa and Hilton is also relatively enriched in Co (Cave et al., 2020a; Cave et al., 2020b), which may indicate that fractionation effects of Co among pyrite and other sulfide phases were relatively minor and that Cu-mineralization at George Fisher formed from relatively Co-rich fluids coeval with Mount Isa and Hilton Cu.

5.4 Implications of pyrite geochemistry at the George Fisher deposit

The paragenetic evolution of pyrite TE geochemistry at George Fisher is consistent with a multi-stage mineralizing system, which supports previous petrographic, structural, mineralogical, geochemical, and isotopic studies (Valenta, 1994; Chapman, 2004; Murphy, 2004; Rieger et al., 2020a; Rieger et al., 2021). The chemistry of Py-1 most closely resembles pyrite from undeformed CD-type deposits of the northern Carpentaria province, which formed *via* host rock replacement during burial diagenesis (e.g., Spinks et al., 2021; Magnall et al., 2022). Later ore forming events (ore stage 2 and 3) replaced, recycled, and overprinted pre-existing mineralization and led to the redistribution and upgrading, as well as addition of new metals (i.e., Cu) at George Fisher, which are captured by the distinct TE geochemistry of Py-2 and Py-3 (Figures 6–11, 14). The enrichment of ore stage 1 related elements (Ag, Tl, and Pb) in un-/weakly-mineralized rocks at George Fisher may indicate more widespread fluid flow and alteration during ore stage 1 than during subsequent ore stages (2 and 3). The spatial dimension of ore stages 2 and 3 is more restricted and structurally controlled, which could have resulted in limited trace element dispersion into the surrounding wall rock.

Importantly, TEs that are typically incorporated into diagenetic pyrite (e.g., Mo, Co, Ni) are fairly uniform in Py-0 from George Fisher and the Shovel Flats drill hole, whereas those with an ore stage 1 affinity are anomalous, particularly in Py-0_{GF} (e.g., Tl, Zn, Pb). It is possible that alteration during ore stage 1 produced micro- to nano-scale TE enriched pyrite overgrowths that nucleated on diagenetic Py-0 beyond the ore bodies at George Fisher (*cf.*, Magnall et al., 2022). The identification of distal, potentially fine-scale, pyrite TE halos would help to improve the understanding of fluid flow and alteration in distal parts of basin hosted mineral systems and to de-risk mineral exploration programs. Future studies should refine the 3D distribution of such pyrite TE halos around the George Fisher deposit and employ higher resolution (10–100 nm scale) analyses of pyrite to determine the nature of this TE anomalism.

6 Conclusion

Pyrite TE chemistry from the George Fisher (Zn-Pb-Ag) deposit and the unmineralized host lithologies (Urquhart Shale Formation) has been influenced by a variety of processes. Diagenetic pyrite from the Urquhart Shale Formation has a broadly similar composition to other Proterozoic sedimentary

and diagenetic pyrite. Importantly, compositional variability of some elements (Ni, Zn, and Tl) in diagenetic pyrite relative to literature data may be related to initial subbasin geochemistry (Ni-depletion) and anomalism (Zn- and Tl-enrichment) in the distal parts of the hydrothermal system. The composition of pyrite is distinct between the individual ore stages. Ore stage 1 pyrite (Py-1) formed during syn-diagenetic mineralization and contains a suite of TEs (As, Sb, Tl, Ag, and Cu) involved in coupled heterovalent substitution. Ore stage 2 pyrite (Py-2) formed *via* replacement and recrystallization of previous pyrite, which resulted in expulsion of less compatible TEs (e.g., Tl) and more Co- and Ni-dominated TE signatures. Ore stage 3 pyrite (Py-3) formed from a separate hydrothermal event and resulted in Co-Ni-Cu-dominant TE signatures. This study has shown that paragenetically constrained pyrite TE data can be an important tool for understanding the formation of complex, multi-stage massive sulfide systems and that it can potentially assist in recognizing hydrothermal anomalies around sedimentary basin-hosted mineral systems.

Data availability statement

The datasets presented in this study can be found in online repositories. The names of the repository/repositories and accession number(s) can be found below: GFZ data services <https://doi.org/10.5880/GFZ.3.1.2022.004>.

Author contributions

JM, SG, and PR designed the project. PR prepared the samples and performed petrography. MO and PR conducted LA-ICP-MS analyses and data reduction. The data was interpreted by PR supported by discussions with JM, SG, and MO. PR wrote the manuscript with contributions from JM, SG, and MO.

References

- Bajwah, Z. U., Seccombe, P. K., and Offler, R. (1987). Trace element distribution Co:Ni ratios and Genesis of the big cadia iron-copper deposit, new south wales, Australia. *Min. Deposita* 22, 292–300. doi:10.1007/bf00204522
- Bell, T. H., and Hickey, K. A. (1998). Multiple deformations with successive subvertical and subhorizontal axial planes in the Mount Isa region; their impact on geometric development and significance for mineralization and exploration. *Econ. Geol.* 93, 1369–1389. doi:10.2113/gsecongeo.93.8.1369
- Berner, R. A. (1984). Sedimentary pyrite formation: An update. *Geochim. Cosmochim. Acta* 48, 605–615. doi:10.1016/0016-7037(84)90089-9
- Bethke, P. M., and Barton, P. B. (1971). Distribution of some minor elements between coexisting sulfide minerals. *Econ. Geol.* 66, 140–163. doi:10.2113/gsecongeo.66.1.140
- Betts, P. G., Armit, R. J., Stewart, J., Aitken, A. R. A., Ailleres, L., Donchak, P., et al. (2016). Australia and Nuna. *Nuna. Geol. Soc. Lond. Spec. Publ.* 424, 47–81. doi:10.1144/SP424.2
- Betts, P. G., Giles, D., Lister, G. S., and Frick, L. R. (2002). Evolution of the Australian lithosphere. *Aust. J. Earth Sci.* 49, 661–695. doi:10.1046/j.1440-0952.2002.00948.x
- Cave, B., Lilly, R., and Barovich, K. (2020a). Textural and geochemical analysis of chalcopyrite, galena and sphalerite across the Mount Isa Cu to Pb-Zn transition: Implications for a zoned Cu-Pb-Zn system. *Ore Geol. Rev.* 124, 103647. doi:10.1016/j.oregeorev.2020.103647
- Cave, B., Lilly, R., and Hong, W. (2020b). The effect of co-crystallising sulphides and precipitation mechanisms on sphalerite geochemistry: A case study from the Hilton Zn-Pb (Ag) deposit, Australia. *Minerals* 10, 797. doi:10.3390/min10090797
- Chapman, L. H. (1999). Geology and Genesis of the George Fisher Zn-Pb-Ag deposit Mount Isa, Australia. PhD thesis. Singapore: James Cook University.
- Chapman, L. H. (2004). Geology and mineralization styles of the George Fisher Zn-Pb-Ag deposit, Mount Isa, Australia. *Econ. Geol.* 99, 233–255. doi:10.2113/gsecongeo.99.2.233
- Chappaz, A., Lyons, T. W., Gregory, D. D., Reinhard, C. T., Gill, B. C., Li, C., et al. (2014). Does pyrite act as an important host for molybdenum in modern and ancient euxinic sediments? *Geochim. Cosmochim. Acta* 126, 112–122. doi:10.1016/j.gca.2013.10.028
- Chouinard, A., Paquette, J., and Williams-Jones, A. E. (2005). Crystallographic controls on trace-element incorporation in auriferous pyrite from the Pascua epithermal high-sulfidation deposit, Chile–Argentina. *Can. Mineral.* 43, 951–963. doi:10.2113/gscanmin.43.3.951
- Connors, K. A., and Page, R. W. (1995). Relationships between magmatism, metamorphism and deformation in the Western Mount Isa inlier, Australia. *Precambrian Res.* 71, 131–153. doi:10.1016/0301-9268(94)00059-Z
- Cook, N. J., Ciobanu, C. L., and Mao, J. (2009). Textural control on gold distribution in as-free pyrite from the dongping, huangtuliang and houguo gold deposits, north China craton (hebei province, China). *Chem. Geol.* 264, 101–121. doi:10.1016/j.chemgeo.2009.02.020
- Craig, J. R., and Vokes, F. M. (1993). The metamorphism of pyrite and pyritic ores: An overview. *Mineral. Mag.* 57, 3–18. doi:10.1180/minmag.1993.057.386.02
- Deditius, A. P., and Reich, M. (2016). Constraints on the solid solubility of Hg, Tl, and Cd in arsenian pyrite. *Am. Mineral.* 101, 1451–1459. doi:10.2138/am-2016-5603
- Deditius, A. P., Utsunomiya, S., Reich, M., Kesler, S. E., Ewing, R. C., Hough, R., et al. (2011). Trace metal nanoparticles in pyrite. *Ore Geol. Rev.* 42, 32–46. doi:10.1016/j.oregeorev.2011.03.003

Funding

This project was provided by a Helmholtz Recruitment Initiative grant to SG.

Acknowledgments

The geology teams at Mount Isa Mines George Fisher operation and Mount Isa Mines Resource Development are thanked for the support during field work and for access to drill cores. P. Rea from Mount Isa Mines Resource Development is warmly acknowledged for an early review of this manuscript. We would also like to thank R. Lilly for support during initializing the project and for fruitful discussions throughout. The technical assistance by U. Dittmann and E. Lewerenz (sample preparation) and the help by F. Wilke with EPMA analyses are warmly acknowledged. Furthermore, we would like to thank M. Reich and S. Hayes for editorial handling and S. Hayes, J. Mavrogenes, L. Danyushevsky, and an anonymous reviewer for their comprehensive reviews that helped to improve this manuscript.

Conflict of interest

The authors declare that the research was conducted in the absence of any commercial or financial relationships that could be construed as a potential conflict of interest.

Publisher's note

All claims expressed in this article are solely those of the authors and do not necessarily represent those of their affiliated organizations, or those of the publisher, the editors and the reviewers. Any product that may be evaluated in this article, or claim that may be made by its manufacturer, is not guaranteed or endorsed by the publisher.

- Deditius, A. P., Utsunomiya, S., Renock, D., Ewing, R. C., Ramana, C. V., Becker, U., et al. (2008). A proposed new type of arsenian pyrite: Composition, nanostructure and geological significance. *Geochim. Cosmochim. Acta* 72, 2919–2933. doi:10.1016/j.gca.2008.03.014
- Dehnavi, A. S., McFarlane, C. R. M., Lentz, D. R., and Walker, J. A. (2018). Assessment of pyrite composition by LA-ICP-MS techniques from massive sulfide deposits of the Bathurst Mining Camp, Canada: From textural and chemical evolution to its application as a vectoring tool for the exploration of VMS deposits. *Ore Geol. Rev.* 92, 656–671. doi:10.1016/j.oregeorev.2017.10.010
- Del Real, I., Thompson, J. F. H., Simon, A. C., and Reich, M. (2020). Geochemical and isotopic signature of pyrite as a proxy for fluid source and evolution in the Candelaria-Punta del Cobre iron oxide copper-gold district, Chile. *Econ. Geol.* 115, 1493–1518. doi:10.5382/econgeo.4765
- Dellwig, O., Leipe, T., März, C., Glockzin, M., Pollehne, F., Schnetger, B., et al. (2010). A new particulate Mn–Fe–P-shuttle at the redoxcline of anoxic basins. *Geochim. Cosmochim. Acta* 74, 7100–7115. doi:10.1016/j.gca.2010.09.017
- Ding, T., Wang, J., Tan, T., Zhang, C., Ye, X., and Hao, X. (2021). Sulfur isotopic and trace-element compositions of pyrite from the Zankan iron deposit, West Kunlun Orogenic Belt, China: Possible Early Cambrian banded iron formations. *Geol. J.* 56, 5738–5754. doi:10.1002/gj.4270
- Domagala, J., Southgate, P. N., McConachie, B. A., and Pidgeon, B. A. (2000). Evolution of the palaeoproterozoic prize, Gun and lower Loretta supersequences of the surprise Creek formation and Mt Isa group. *Aust. J. Earth Sci.* 47, 485–507. doi:10.1046/j.1440-0952.2000.00796.x
- D’Orazio, M., Biagioni, C., Dini, A., and Vezzoni, S. (2017). Thallium-rich pyrite ores from the apuan alps, tuscany, Italy: Constraints for their origin and environmental concerns. *Mineral. Depos.* 52, 687–707. doi:10.1007/s00126-016-0697-1
- Eldridge, C. S., Williams, N., and Walshe, J. L. (1993). Sulfur isotope variability in sediment-hosted massive sulfide deposits as determined using the ion microprobe SHRIMP; II, A study of the HVC Deposit at McArthur River, Northern Territory, Australia. *Econ. Geol.* 88, 1–26. doi:10.2113/gsecongeo.88.1.1
- Fike, D. A., Bradley, A. S., and Rose, C. V. (2015). Rethinking the ancient sulfur cycle. *Annu. Rev. Earth Planet. Sci.* 43, 593–622. doi:10.1146/annurev-earth-060313-054802
- Gadd, M. G., Layton-Matthews, D., Peter, J. M., and Paradis, S. J. (2016). The world-class howard’s pass SEDEX Zn–Pb district, selwyn basin, yukon. Part I: Trace element compositions of pyrite record input of hydrothermal, diagenetic, and metamorphic fluids to mineralization. *Min. Depos.* 51, 319–342. doi:10.1007/s00126-015-0611-2
- George, L. L., Biagioni, C., D’Orazio, M., and Cook, N. J. (2018). Textural and trace element evolution of pyrite during greenschist facies metamorphic recrystallization in the southern Apuan Alps (Tuscany, Italy): Influence on the formation of Tl-rich sulfosalt melt. *Ore Geol. Rev.* 102, 59–105. doi:10.1016/j.oregeorev.2018.08.032
- George, L. L., Cook, N. J., and Ciobanu, C. L. (2016). Partitioning of trace elements in co-crystallized sphalerite–galena–chalcopyrite hydrothermal ores. *Ore Geol. Rev.* 77, 97–116. doi:10.1016/j.oregeorev.2016.02.009
- Gibson, G. M., Hutton, L. J., and Holzschuh, J. (2017). Basin inversion and supercontinent assembly as drivers of sediment-hosted Pb–Zn mineralization in the Mount Isa region, northern Australia. *J. Geol. Soc. Lond.* 174, 773–786. doi:10.1144/jgs2016-105
- Giles, D., Betts, P., and Lister, G. (2002). Far-field continental backarc setting for the 1.80–1.67 Ga basins of northeastern Australia. *Geology* 30, 823–826. doi:10.1130/0091-7613(2002)030<0303C0823:FFCBSF%3E2.0.CO;2
- Glencore (2021). Resources and reserves report. Available At: https://www.glencore.com/dam/jcr:3290c4f8-ba0c-4783-8cda-7bff4bd58c6b/2021-GLEN_Resources-and-Reserves-report.pdf.
- Grant, H. L. J., Hannington, M. D., Petersen, S., Frische, M., and Fuchs, S. H. (2018). Constraints on the behavior of trace elements in the actively-forming TAG deposit, Mid-Atlantic Ridge, based on LA-ICP-MS analyses of pyrite. *Chem. Geol.* 498, 45–71. doi:10.1016/j.chemgeo.2018.08.019
- Gregory, D. D., Cracknell, M. J., Large, R. R., McGoldrick, P., Kuhn, S., Maslennikov, V. V., et al. (2019). Distinguishing ore deposit type and barren sedimentary pyrite using laser ablation-inductively coupled plasma-mass spectrometry trace element data and statistical analysis of large data sets. *Econ. Geol.* 114, 771–786. doi:10.5382/econgeo.4654
- Hannan, K. W., Golding, S. D., Herbert, H. K., and Krouse, H. R. (1993). Contrasting alteration assemblages in metabasites from Mount Isa, Queensland; implications for copper ore Genesis. *Econ. Geol.* 88, 1135–1175. doi:10.2113/gsecongeo.88.5.1135
- Hayward, N., Magnall, J. M., Taylor, M., King, R., McMillan, N., and Gleeson, S. A. (2021). The Teena Zn–Pb deposit (McArthur Basin, Australia). Part I: Syndiagenetic base metal sulfide mineralization related to dynamic subbasin evolution. *Econ. Geol.* 116, 1743–1768. doi:10.5382/econgeo.4846
- Heinrich, C. A., Andrew, A. S., Wilkins, R. W. T., and Patterson, D. J. (1989). A fluid inclusion and stable isotope study of synmetamorphic copper ore formation at Mount Isa, Australia. *Econ. Geol.* 84, 529–550. doi:10.2113/gsecongeo.84.3.529
- Helz, G. R., Miller, C. V., Charnock, J. M., Mosselmann, J. F. W., Patrick, R. A. D., Garner, C. D., et al. (1996). Mechanism of molybdenum removal from the sea and its concentration in black shales: EXAFS evidence. *Geochim. Cosmochim. Acta* 60, 3631–3642. doi:10.1016/0016-7037(96)00195-0
- Huerta-Diaz, M. A., and Morse, J. W. (1990). A quantitative method for determination of trace metal concentrations in sedimentary pyrite. *Mar. Chem.* 29, 119–144. doi:10.1016/0304-4203(90)90009-2
- Huerta-Diaz, M. A., and Morse, J. W. (1992). Pyritization of trace metals in anoxic marine sediments. *Geochim. Cosmochim. Acta* 56, 2681–2702. doi:10.1016/0016-7037(92)90353-K
- Huston, D. L., Sie, S. H., Suter, G. F., Cooke, D. R., and Both, R. A. (1995). Trace elements in sulfide minerals from eastern Australian volcanic-hosted massive sulfide deposits; Part I, Proton microprobe analyses of pyrite, chalcopyrite, and sphalerite, and Part II, Selenium levels in pyrite; comparison with delta 34 S values and implications for the source of sulfur in volcanogenic hydrothermal systems. *Econ. Geol.* 90, 1167–1196. doi:10.2113/gsecongeo.90.5.1167
- Jackson, M. J., Scott, D. L., and Rawlings, D. J. (2000). Stratigraphic framework for the leichhardt and calvert superbasins: Review and correlations of the pre-1700 Ma successions between Mt Isa and McArthur river. *Aust. J. Earth Sci.* 47, 381–403. doi:10.1046/j.1440-0952.2000.00789.x
- Keith, M., Häckel, F., Haase, K. M., Schwarz-Schampera, U., and Klemd, R. (2016). Trace element systematics of pyrite from submarine hydrothermal vents. *Ore Geol. Rev.* 72, 728–745. doi:10.1016/j.oregeorev.2015.07.012
- Kusebauch, C., Gleeson, S. A., and Oelze, M. (2019). Coupled partitioning of Au and as into pyrite controls formation of giant Au deposits. *Sci. Adv.* 5, eaav5891. doi:10.1126/sciadv.aav5891
- Large, R. R., Bull, S. W., Cooke, D. R., and McGoldrick, P. J. (1998). A genetic model for the HVC Deposit, Australia; based on regional sedimentology, geochemistry, and sulfide-sediment relationships. *Econ. Geol.* 93, 1345–1368. doi:10.2113/gsecongeo.93.8.1345
- Large, R. R., Halpin, J. A., Danyushevsky, L. V., Maslennikov, V. V., Bull, S. W., Long, J. A., et al. (2014). Trace element content of sedimentary pyrite as a new proxy for deep-time ocean–atmosphere evolution. *Earth Planet. Sci. Lett.* 389, 209–220. doi:10.1016/j.epsl.2013.12.020
- Large, R. R., Mukherjee, I., Gregory, D. D., Steadman, J. A., Maslennikov, V. V., and Meffre, S. (2017). Ocean and atmosphere geochemical proxies derived from trace elements in marine pyrite: Implications for ore Genesis in sedimentary basins. *Econ. Geol.* 112, 423–450. doi:10.2113/gsecongeo.112.2.423
- Leach, D. L., Bradley, D. C., Huston, D., Pisarevsky, S. A., Taylor, R. D., and Gardoll, S. J. (2010). Sediment-hosted lead-zinc deposits in earth history. *Econ. Geol.* 105, 593–625. doi:10.2113/gsecongeo.105.3.593
- Leach, D. L., Sangster, D. F., Kelley, K. D., Large, R. R., Garven, G., Allen, C. R., et al. (2005). Sediment-hosted lead-zinc deposits: A global perspective. *Econ. Geol.* 100, 561–607. doi:10.5382/AV100.18
- Li, S., Wang, X. C., Hu, S. Y., Guagliardo, P., Kilburn, M., Golding, S. D., et al. (2022). Recognition of a widespread Paleoproterozoic hydrothermal system in the southern McArthur Basin, northern Australia, by *in-situ* analysis of fine-grained pyrite and spatially-associated solid bitumen in the Lamont Pass palaeohigh. *Ore Geol. Rev.* 144, 104834. doi:10.1016/j.oregeorev.2022.104834
- Lyons, T. W., Reinhard, C. T., and Planavsky, N. J. (2014). The rise of oxygen in Earth’s early ocean and atmosphere. *Nature* 506, 307–315. doi:10.1038/nature13068
- Magnall, J. M., Gleeson, S. A., Hayward, N., and Oelze, M. (2022). Using whole rock and *in situ* pyrite chemistry to evaluate authigenic and hydrothermal controls on trace element variability in a Zn mineralized Proterozoic subbasin. *Geochim. Cosmochim. Acta* 318, 366–387. doi:10.1016/j.gca.2021.12.001
- Magnall, J. M., Gleeson, S. A., Hayward, N., and Rocholl, A. (2020). Massive sulfide Zn deposits in the Proterozoic did not require euxinia. *Geochem. Perspect. Lett.* 13, 19–24. doi:10.7185/geochemlet.2008
- Magnall, J. M., Hayward, N., Gleeson, S. A., Schleicher, A., Dalrymple, I., King, R., et al. (2021). The Teena Zn–Pb deposit (McArthur basin, Australia). Part II: Carbonate replacement sulfide mineralization during burial diagenesis - implications for mineral exploration. *Econ. Geol.* 116, 1769–1801. doi:10.5382/econgeo.4845
- Maslennikov, V. V., Maslennikova, S. P., Large, R. R., and Danyushevsky, L. V. (2009). Study of trace element zonation in vent chimneys from the silurian yaman-kasy volcanic-hosted massive sulfide deposit (southern urals, Russia) using laser ablation-inductively coupled plasma mass spectrometry (LA-ICPMS). *Econ. Geol.* 104, 1111–1141. doi:10.2113/gsecongeo.104.8.1111
- Mathias, B. V., and Clark, G. J. (1975). Mount Isa copper and silver-lead-zinc orebodies—Isa and Hilton mines. *Econ. Geol. Aust. P. N. G. Aust. Inst. Min. Metall.* 1, 351–372.
- McClay, K. R. (1979). Folding in silver-lead-zinc orebodies, Mount Isa, Australia. *Trans. Inst. Min. Metall. Sect. B Appl. Earth Sci.* 88, B5–B14.
- McGoldrick, P. J., and Keays, R. R. (1990). Mount Isa copper and lead-zinc-silver ores; coincidence or cogenesis? *Econ. Geol.* 85, 641–650. doi:10.2113/gsecongeo.85.3.641
- McGoldrick, P., Winefield, P., Bull, S., Selley, D., and Scott, R. (2010). Sequences, synsedimentary structures, and sub-basins: The where and when of SEDEX zinc systems in the southern McArthur basin, Australia. *Soc. Econ. Geol. Spec. Publ.* 15, 1–23. doi:10.5382/SP.15.2.02
- Morse, J. W., and Luther, G. W., III (1999). Chemical influences on trace metal–sulfide interactions in anoxic sediments. *Geochim. Cosmochim. Acta* 63, 3373–3378. doi:10.1016/S0016-7037(99)00258-6

- Murphy, T. E. (2004). Structural and stratigraphic controls on mineralization at the George Fisher Zn-Pb-Ag Deposit, northwest Queensland, Australia. PhD thesis. Queensland, Australia: James Cook University.
- Nameroff, T. J., Balistreri, L. S., and Murray, J. W. (2002). Suboxic trace metal geochemistry in the eastern tropical North Pacific. *Geochim. Cosmochim. Acta* 66, 1139–1158. doi:10.1016/S0016-7037(01)00843-2
- Neudert, M. (1983). A depositional model for the Upper Mount Isa Group and implications for ore formation. PhD thesis. Australia: Australian National University.
- Nozaki, T., Nagase, T., Ushikubo, T., Shimizu, K., and Ishibashi, J. I. (2021). Microbial sulfate reduction plays an important role at the initial stage of SubSeafloor sulfide mineralization. *Geology* 49, 222–227. doi:10.1130/G47943.1
- Page, R. W., and Bell, T. H. (1986). Isotopic and structural responses of granite to successive deformation and metamorphism. *J. Geol.* 94, 365–379. doi:10.1086/629035
- Page, R. W., Jackson, M. J., and Krassay, A. A. (2000). Constraining sequence stratigraphy in north Australian basins: SHRIMP U–Pb zircon geochronology between Mt Isa and McArthur river. *Aust. J. Earth Sci.* 47, 431–459. doi:10.1046/j.1440-0952.2000.00797.x
- Page, R. W., and Sweet, I. P. (1998). Geochronology of basin phases in the Western Mt Isa inlier, and correlation with the McArthur basin. *Aust. J. Earth Sci.* 45, 219–232. doi:10.1080/08120099808728383
- Painter, M. G. M., Golding, S. D., Hannan, K. W., and Neudert, M. K. (1999). Sedimentologic, petrographic, and sulfur isotope constraints on fine-grained pyrite formation at Mount Isa Mine and environs, Northwest Queensland, Australia. *Econ. Geol.* 94, 883–912. doi:10.2113/gsecongeo.94.6.883
- Painter, M. G. M. (2003). The geochemical and mineralogical haloes around the Mt Isa base metal orebodies. PhD thesis. Australia: University of Queensland.
- Paton, C., Hellstrom, J., Paul, B., Woodhead, J., and Hergt, J. (2011). Iolite: Freeware for the visualisation and processing of mass spectrometric data. *J. Anal. At. Spectrom.* 26, 2508–2518. doi:10.1039/C1JA10172B
- Perkins, W. G. (1997). Mount Isa lead-zinc orebodies: Replacement lodes in a zoned syndeformational copper-lead-zinc system? *Ore Geol. Rev.* 12, 61–110. doi:10.1016/S0169-1368(97)00004-8
- Piercy, S. J. (2015). A semipermeable interface model for the Genesis of subseafloor replacement-type volcanogenic massive sulfide (VMS) deposits. *Econ. Geol.* 110, 1655–1660. doi:10.2113/econgeo.110.7.1655
- Qian, G., Brugger, J., Testemale, D., Skinner, W., and Pring, A. (2013). Formation of As(II)-pyrite during experimental replacement of magnetite under hydrothermal conditions. *Geochim. Cosmochim. Acta* 100, 1–10. doi:10.1016/j.gca.2012.09.034
- Raiswell, R., and Plant, J. (1980). The incorporation of trace elements into pyrite during diagenesis of black shales, Yorkshire, England. *Econ. Geol.* 75, 684–699. doi:10.2113/gsecongeo.75.5.684
- Reich, M., Kesler, S. E., Utsunomiya, S., Palenik, C. S., Chryssoulis, S. L., and Ewing, R. C. (2005). Solubility of gold in arsenian pyrite. *Geochim. Cosmochim. Acta* 69, 2781–2796. doi:10.1016/j.gca.2005.01.011
- Reich, M., Simon, A. C., Deditius, A., Barra, F., Chryssoulis, S., Lagas, G., et al. (2016). Trace element signature of pyrite from the los colorados iron oxide-apatite (IOA) deposit, Chile: A missing link between andean IOA and iron oxide copper-gold systems? *Econ. Geol.* 111, 743–761. doi:10.2113/econgeo.111.3.743
- Rieger, P., Magnall, J. M., Gleeson, S. A., Lilly, R., Rocholl, A., and Kusebauch, C. (2020a). Sulfur isotope constraints on the conditions of pyrite formation in the paleoproterozoic Urquhart Shale Formation and George Fisher Zn-Pb-Ag deposit, northern Australia. *Econ. Geol.* 115, 1003–1020. doi:10.5382/econgeo.4726
- Rieger, P., Magnall, J. M., Gleeson, S. A., and Oelze, M. (2022b). *Laser ablation inductively coupled mass spectrometry of pyrite from the paleoproterozoic George Fisher deposit and Urquhart Shale Formation (Mount Isa, Australia)*. Queensland, Australia: GFZ Data Services. doi:10.5880/GFZ.3.1.2022.004
- Rieger, P., Magnall, J. M., Gleeson, S. A., Oelze, M., Wilke, F. D. H., and Lilly, R. (2022a). Differentiating between hydrothermal and diagenetic carbonate using rare Earth element and yttrium (REE+ Y) geochemistry: A case study from the paleoproterozoic George Fisher massive sulfide Zn deposit, Mount Isa, Australia. *Min. Depos.* 57, 187–206. doi:10.1007/s00126-021-01056-1
- Rieger, P., Magnall, J. M., Gleeson, S. A., Schleicher, A. M., Bonitz, M., and Lilly, R. (2020b). *The mineralogical and lithochemical footprint of the George Fisher Zn-Pb-Ag massive sulphide deposit in the Proterozoic Urquhart Shale Formation*. Queensland, Australia: GFZ Data Services. doi:10.5880/GFZ.3.1.2020.003
- Rieger, P., Magnall, J. M., Gleeson, S. A., Schleicher, A. M., Bonitz, M., and Lilly, R. (2021). The mineralogical and lithochemical footprint of the George Fisher Zn-Pb-Ag massive sulphide deposit in the Proterozoic Urquhart Shale Formation, Queensland, Australia. *Chem. Geol.* 560, 119975. doi:10.1016/j.chemgeo.2020.119975
- Rye, D. M., and Williams, N. (1981). Studies of the base metal sulfide deposits at McArthur river, northern territory, Australia: III. The stable isotope geochemistry of the H.Y.C., ridge, and cooley deposits. *Econ. Geol.* 76, 1–26. doi:10.2113/gsecongeo.76.1.1
- Scholz, F. (2018). Identifying oxygen minimum zone-type biogeochemical cycling in Earth history using inorganic geochemical proxies. *Earth-Science Rev.* 184, 29–45. doi:10.1016/j.earscrv.2018.08.002
- Scholz, F., and Neumann, T. (2007). Trace element diagenesis in pyrite-rich sediments of the Achterwasser lagoon, SW Baltic Sea. *Mar. Chem.* 107, 516–532. doi:10.1016/j.marchem.2007.08.005
- Southgate, P. N., Neumann, N. L., and Gibson, G. M. (2013). Depositional systems in the Mt Isa inlier from 1800 Ma to 1640 Ma: Implications for Zn–Pb–Ag mineralisation. *Aust. J. Earth Sci.* 60, 157–173. doi:10.1080/08120099.2013.758176
- Southgate, P. N., Scott, D. L., Sami, T. T., Domagala, J., Jackson, M. J., James, N. P., et al. (2000). Basin shape and sediment architecture in the Gun supersequence: A strike-slip model for Pb–Zn–Ag ore Genesis at Mt Isa. *Aust. J. Earth Sci.* 47, 509–531. doi:10.1046/j.1440-0952.2000.00792.x
- Spinks, S. C., Pearce, M. A., Liu, W., Kunzmann, M., Ryan, C. G., Moorhead, G. F., et al. (2021). Carbonate replacement as the principal ore formation process in the proterozoic McArthur river (HYC) sediment-hosted Zn-Pb deposit, Australia. *Econ. Geol.* 116, 693–718. doi:10.5382/econgeo.4793
- Valenta, R. (1994). Deformation of host rocks and stratiform mineralization in the Hilton Mine area, Mt Isa. *Aust. J. Earth Sci.* 41, 429–443. doi:10.1080/08120099408728153
- Vorlicek, T. P., Helz, G. R., Chappaz, A., Vue, P., Vezina, A., and Hunter, W. (2018). Molybdenum burial mechanism in sulfidic sediments: Iron-sulfide pathway. *ACS Earth Sp. Chem.* 2, 565–576. doi:10.1021/acsearthspchem.8b00016
- Vorlicek, T. P., Kahn, M. D., Kasuya, Y., and Helz, G. R. (2004). Capture of molybdenum in pyrite-forming sediments: Role of ligand-induced reduction by polysulfides. *Geochim. Cosmochim. Acta* 68, 547–556. doi:10.1016/S0016-7037(03)00444-7
- Woodhead, J. D., Hellstrom, J., Hergt, J. M., Greig, A., and Maas, R. (2007). Isotopic and elemental imaging of geological materials by laser ablation inductively coupled plasma-mass spectrometry. *Geostand. Geoanalytical Res.* 31, 331–343. doi:10.1111/j.1751-908X.2007.00104.x